ON THE PRECIPITATION IN TERNARY Al-Zn-Mg ALLOYS

A THESIS

Presented to

The Faculty of the Graduate Division

by

Pronob Bardhan

In Partial Fulfillment

of the Requirements for the Degree

Master of Science in Metallurgy

Georgia Institute of Technology

February, 1968

ON THE PRECIPITATION IN TERNARY Al-Zn-Mg ALLOYS

Approved:

Chairman

Date approved by Chairman: 3/27/68

In presenting the dissertation as a partial fulfillment of the requirements for an advanced degree from the Georgia Institute of Technology, I agree that the Library of the Institute shall make it available for inspection and circulation in accordance with its regulations governing materials of this type. I agree that permission to copy from, or to publish from, this dissertation may be granted by the professor under whose direction it was written, or, in his absence, by the Dean of the Graduate Division when such copying or publication is solely for scholarly purposes and does not involve potential financial gain. It is understood that any copying from, or publication of, this dissertation which involves potential financial gain will not be allowed without written permission.

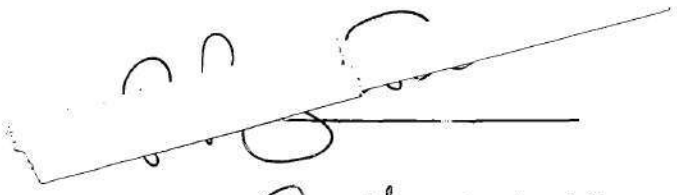

April 23, 1968

3/17/65
b

ACKNOWLEDGMENTS

The author is deeply indebted to his thesis advisor, Dr. Edgar A. Starke, Jr., for suggesting this research and for his invaluable encouragement and guidance throughout this project.

It gives the author great pleasure to thank Drs. Bruce LeFevre and Stephen Spooner for having taken time off from their many and pressing duties to review this work. Their interest and constructive criticism is greatly appreciated.

Finally, the assistance and learned counsel given the author by his colleagues in the Department is gratefully acknowledged.

TABLE OF CONTENTS

LIST OF TABLES

LIST OF FIGURES

LIST OF FIGURES (Continued)

SUMMARY

The decomposition of two Al-Zn-Mg alloys was studied using hardness measurements, high-angle x-ray diffraction, and small-angle x-ray scattering measurements.

Ageing characteristics in the ternary system were determined as a function of time, ageing temperature, and composition. Strength was correlated to the zone sizes evaluated from the small-angle scattering curves. It was found that the nucleation of the intermediate η' precipitate required a critical zone size.

The role of magnesium during the ageing process has been found to be two-fold; first, magnesium affects the initial clustering of zinc to form zones and governs the concentration of zinc in the zones, and second, magnesium acts as a reversible vacancy trap and the latter plays the important role of aiding the ageing phenomenon in the later stages.

CHAPTER I

INTRODUCTION

The age hardening phenomonon was first discovered by A. Wilm in 1905. It is found to occur in alloy systems which can form supersaturated solid solutions and then reject the solute when aged at low or intermediate temperatures. Binary or ternary alloys in which the solid solubility of one metal in another decreases with temperature are often subjected to this treatment. The complete heat treatment consists of first "solutionizing" by heating into the single-phase region, holding there long enough to dissolve all existing soluble precipitate particles, and then rapidly quenching into the two-phase region. The rapidity of the quench prevents the formation of the equilibrium precipitate and results in a supersaturated solid solution. Subsequent ageing at low temperatures results in the formation of transition structures called the Guinier-Preston zones, after the men who first identified these structures by x-ray diffraction. The strengthening that occurs on ageing is due to the formation of the Guinier-Preston zones, or due to the appearance of an intermediate precipitate. This is due to the fact that the precipitates have a higher shear modulus than the matrix or lead to local distortions and strain fields which impede the motion of dislocations. Age hardening is found to occur fairly frequently in aluminum alloys.

The high tensile properties obtained by ageing ternary aluminum-zinc-magnesium alloys was first reported by Sander and Meissner[1,2]. They ob-

served that these alloys had a greater strength than the known aluminum alloys; however, the susceptibility to stress corrosion cracking of the ternary alloys prevented their commercial development. During World War II when a great demand arose for new materials, interest was revived again in these alloys. The studies that followed led to the discovery that the addition of manganese, chromium, and copper appreciably enhanced the resistance to stress corrosion cracking. The aluminum-zinc-magnesium alloys soon found widespread applications, especially in the production of pressure vessels, military vehicles (for example, tanks), cryogenic apparatus, aircrafts, and missiles.

Since the development of the alloys numerous investigations have been made on isolated alloys belonging to the ternary system, to determine the nature of the ageing process. The techniques used to study these changes induced by heat treatment have, in general, been of two types: the structural approach in which the methods of electron microscopy or x-ray diffraction are applied to the study of the alloy structure, and the kinetic approach in which the variation of some property such as hardness or electrical resistivity is measured as a function of time and temperature of ageing. Chapter II is a comprehensive review of the results of some of these investigations.

As will be seen later in this review, these studies have established only one aspect of the ageing process, that is, the ageing phenomenon is fairly complex. Furthermore, since individual techniques have been applied independently of one another, the one-to-one correspondence between structure and property which has been assumed in most cases may be questioned. The studies have attempted to follow only changes in mechanical property

with ageing, or, they have concentrated on structural changes alone. In view of this, a correlation of structure and property during the ageing of Al-Zn-Mg alloys was considered important.

In the present investigation hardness measurements were made as a function of ageing time and temperature. At various intermediate stages the structure was characterized by small-angle scattering measurements, high-angle x-ray diffraction measurements, and electron microscopy. By these means it is felt that a more complete understanding of the ageing process in the ternary system will be possible.

CHAPTER II

LITERATURE SURVEY

Phase Relationships

The first equilibrium diagrams for the Al-Zn-Mg system were determined by Koster and co-workers[3,4]. Figure 1 shows the binary phase diagrams of Al-Zn, Al-Mg, and Mg-Zn along with the room temperature phase fields of the ternary system, as determined from metallographic examinations.

X-ray and electrical resistivity studies by Fink and Willey[5] have established the phase relationships at various temperatures for the aluminum rich corner of the ternary system. The phase boundaries at 200°C, determined from such an examination, are shown in Figure 2, and these boundaries are very close to their expected position at room temperature. Both alloys studied in the present investigation, as indicated in Figure 2, are in a region where the primary aluminum solid solution is in equilibrium with the binary $MgZn_2$ phase. Finally, the isotherm of the ternary system at 460°C[6] is shown in Figure 3. This is the temperature chosen for the solution treatment since this temperature lies well within the single-phase field for the alloys under study.

Mechanical Properties

Herenguel and Chaudron[7], working with Al-5 weight percent Mg alloys containing 3, 5, and 7 weight percent Zn, made one of the first attempts to determine the changes in mechanical properties during the ageing of

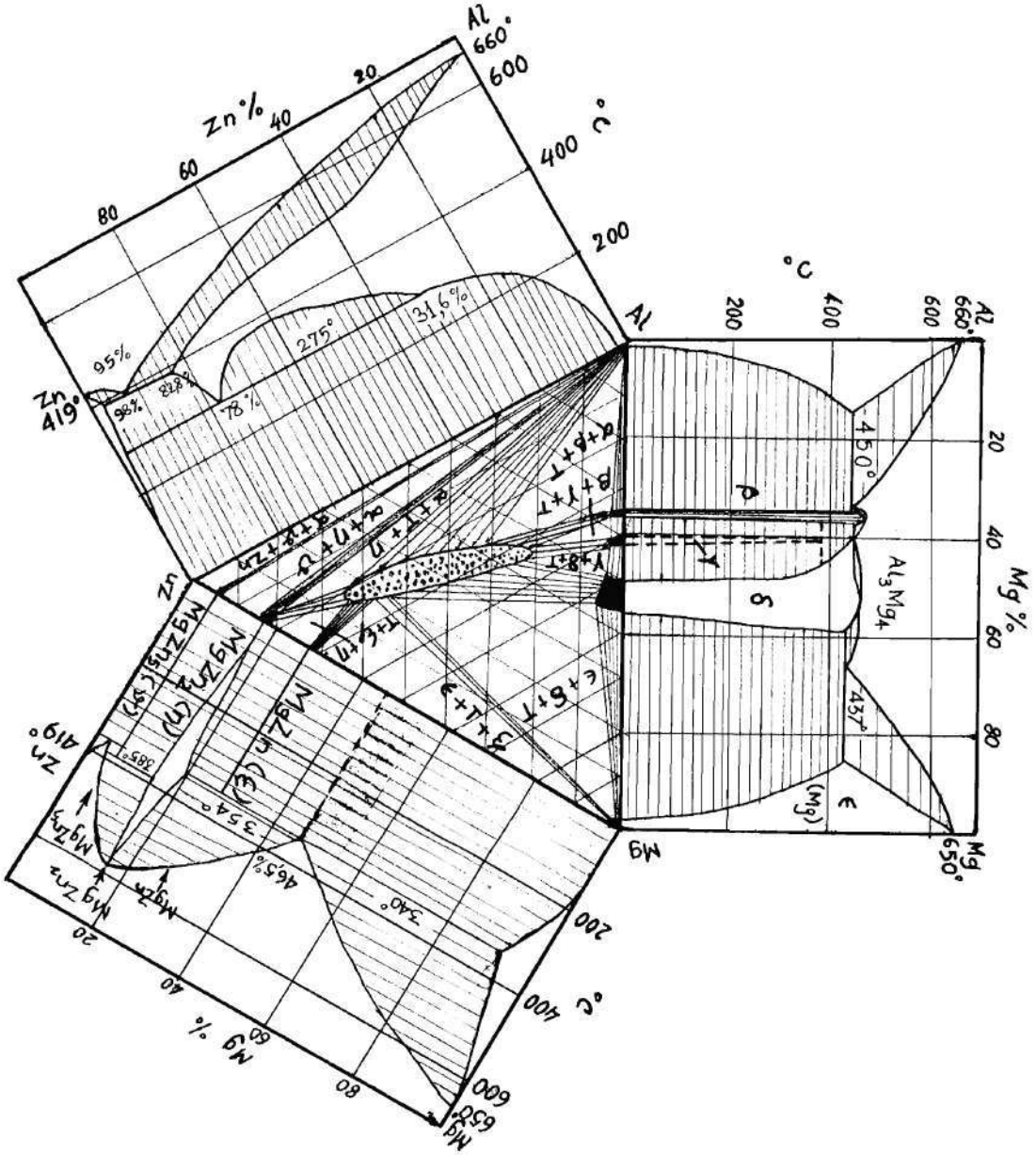

Figure 1. Equilibrium Phase Relationships in the Ternary Al-Zn-Mg System.

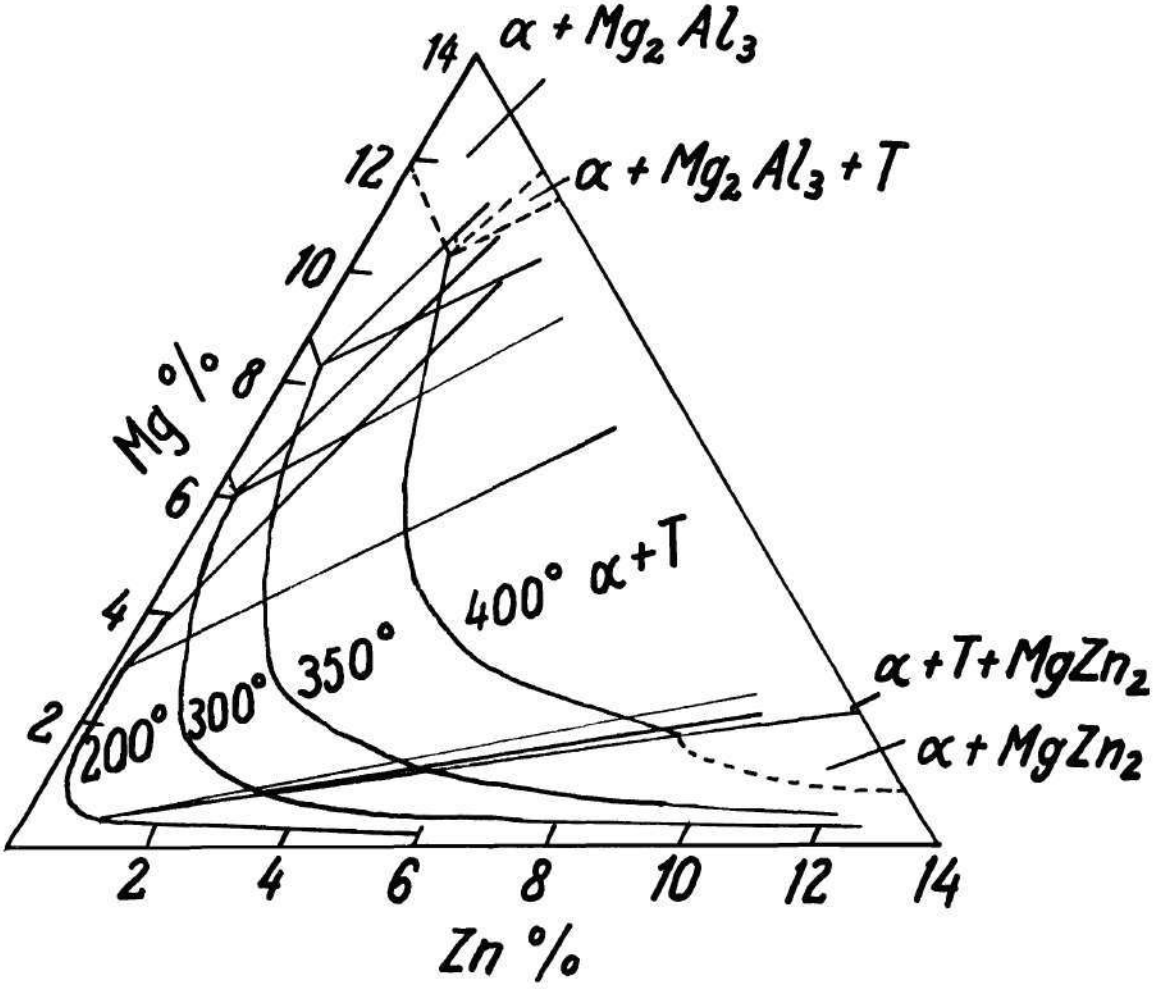

Figure 2. Constitution Diagram of the Ternary Al-Zn-Mg System at Various Temperatures (Fink & Willey).

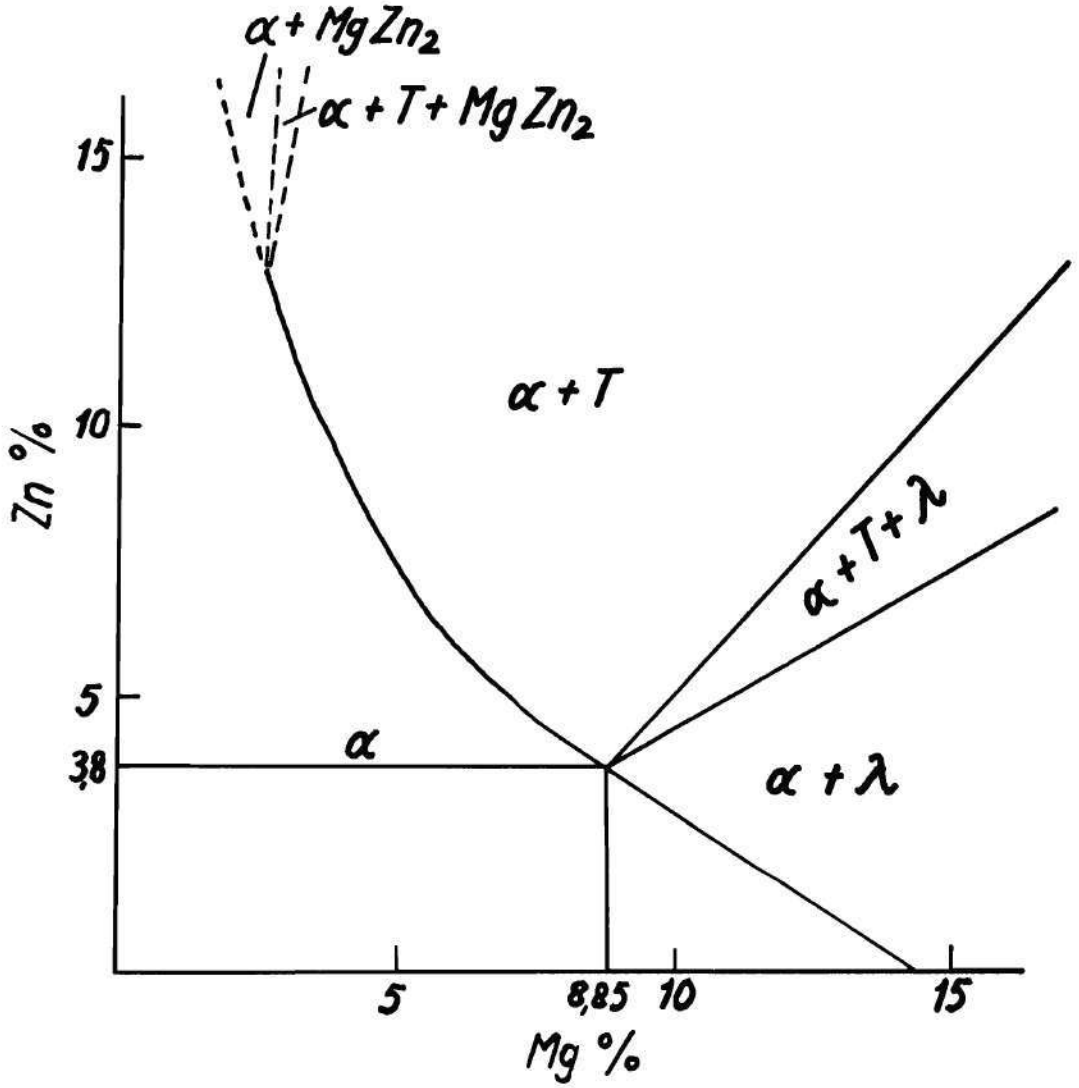

Figure 3. The Isotherm of the Ternary Al-Zn-Mg System at 460°C.

these ternary alloys. For all three alloys the room temperature ageing over a period of 180 days exhibited a linear variation in the hardness versus logarithmic time curve. Graf[8], working on an alloy containing 3 weight percent Mg and 7 weight percent Zn was, however, able to observe a hardness peak when the alloys were aged at 135°C for a period of 6 hours. The peak hardness obtained was approximately three times the as-quenched hardness.

On ageing a slightly more concentrated ternary alloy (8 weight percent Zn and 4 weight percent Mg), Koster and Kam[9] demonstrated the complexity of the ageing process. Ageing was carried out at 20°, 100°, 150°, and 200°C. For 20°C ageing no peak in the hardness curve was seen. At 100°C a two-stage hardening was observed. After a rapid initial increase in hardness (from an as-quenched value of 86 V.P.N. to 124 V.P.N. in one hour), there was no change in the hardness for a period of 2 hours. This was followed by a second-stage in which the hardness reached a peak of 142 V.P.N. in 10 hours. Ageing at 150° and 200°C resulted in hardness peaks of 163 and 152 V.P.N. after periods of 10 hours and 1 hour, respectively.

Realizing the need for a more fundamental understanding of the ageing phenomenon, Polmear[10,11] began a systematic study of the ageing characteristics of a wide range of aluminum-zinc-magnesium alloys. The basic zinc contents in these alloys were 4, 6, and 8 weight percent and the magnesium contents ranged from 0 to 3 weight percent. Ageing was carried out at regular temperature intervals between -20° and +240°C and for periods up to 2 years. Two-stage hardness curves appear for the Al, 4 weight percent Zn, 0.4 weight percent Mg alloy at 60°C, and for the Al, 4 weight per-

cent Zn, 1 weight percent Mg alloy at 90°C. For the Al, 8 weight percent Zn alloys with 0.4 and 1 weight percent Mg contents aged at 90°C there occurs a rapid increase in the hardness immediately after the quench, followed by a slower increase in the hardness. This is followed by rapid hardening which leads to a peak. At 60°C, however, only a linear hardening is observed. From the incubation times at different ageing temperatures, Polmear[10], after the method of Hardy[11], obtained a series of intersecting "C-curves" representing the various stages in the ageing process. The first of the two stages was attributed to the formation of Guinier-Preston zones and the second to the formation of an intermediate precipitate (called the η' precipitate). Using these results Polmear was able to construct the metastable boundary for the G-P zone formation.

Structural Studies

X-ray Studies

One of the earliest investigations to determine the structural changes in the Al, 6 weight percent Zn, 2 weight percent Mg ternary system was made by Mondolfo, Gjostein, and Levinson[12] using Debye-Scherrer, Laue, and Geisler-Hill type techniques. They found that upon ageing at low temperatures (less than 200°C) the binary $MgZn_2$ precipitate formed. The precipitation of the binary phase started with the formation of G-P zones on the matrix {111} planes. This was followed by the formation of a transitional hexagonal lattice similar to $MgZn_2$ possessing different lattice parameters. Ageing above 300°C resulted in the ternary precipitate $(AlZn)_{49}Mg_{32}$, and at intermediate temperatures both phases formed. These conclusions were corroborated by the findings of Graf[13,14] who studied

Al, 7 weight percent Zn, 3 weight percent Mg, and Al, 9 weight percent Zn, 1 weight percent Mg alloy single crystals. Graf[15] inferred from the small-angle scattering patterns that the size of the zones increased with zinc content and the G-P zones in the ternary alloy remained spherical in shape as they do in the Al-Zn binary alloys. An anomalous effect was also observed. The central ring at small angles was narrower and more intense for identical heat-treatments when the proportion of Zn to Mg was increased. This seemed to indicate that the zones causing the small-angle scattering occupied a larger volume fraction as the magnesium content was reduced. A possible explanation for this is that the zone composition altered as the relative amount of zinc was varied. This, however, fails to explain the fact that the large-angle scattered patterns remain unchanged. Guinier[17] proposed another reason for this phenomenon. According to his hypothesis, two types of zones exist at the same time in the ternary system, one containing magnesium and zinc, and the other containing pure or nearly pure zinc. The two-zone hypothesis was used also by Gould and Starke[18] to explain the reversion process in Al, 12.9 weight percent Zn, 0.66 weight percent Mg and Al, 12.8 weight percent Zn, 0.24 weight percent Mg alloys. They found that an unreverted portion persisted in the small-angle scattered intensity even after long reversion times.

It was also observed by Graf that diffuse spots which occurred in the oscillation photographs were not centrally placed. This seemed to suggest the existence of some type of order in the interior of the zones. The ordering of atoms within the zones was established by Schmalzreid and Gerold[16] working on an Al, 6.3 weight percent Zn, 3.5 weight percent Mg alloy. They proposed a structure with alternate {100} planes of zinc and

magnesium. In extending these results to a Al, 7.6 weight percent Zn, 0.86 weight percent Mg alloy, Haberkorn and Gerold[28] discovered that the structure of the ordered zone changes from an AuCu I type to an AuCu II type, with the excess zinc replacing magnesium in the antiphase domain boundary that forms in the latter structure. Also, a tetragonal structure results due to strong lattice distortions in the a-direction in the magnesium-poor alloy.

Electron Microscope Studies

During the early days of electron microscopy, several replica techniques were applied to follow the ageing of the aluminum-zinc-magnesium alloys[20,21,22]. The results obtained by these methods were not in complete agreement with those found by x-ray diffraction. However, in more recent years with the development of a generally applicable electropolishing technique, a range of alloy compositions in this system have been studied.

Early work by Nicholson, Thomas, and Nutting[23] revealed a completely homogeneous type of pre-precipitation. The initial stages of ageing could not be studied however, as the first clusters formed are smaller than the lower limit of the resolution of the electron microscope. Thus, the Guinier-Preston zones could be observed only after they had reached a certain size, generally about 10 Å. The later stages showed the existence of a partially coherent precipitate which, from electron diffraction patterns was found to lie on the {111} planes of the matrix, confirming the results of Mondolfo et al, referred to earlier. It was also observed that the intermediate precipitate was formed by transformation of the coherent zones to the partially incoherent structure which characterizes the intermediate precipitate. It appeared that the smaller zones which remained untrans-

formed around the precipitate then dissolved in the matrix. Therefore, it was suggested that a dispersion hardening mechanism then operated in these alloys when the intermediate precipitate had formed. The alloys were found to soften when coarse precipitates, completely incoherent with the matrix, formed. Further studies by Nicholson, Thomas, and Nutting[25] revealed that dislocations pass through zones and partially coherent precipitates by a process of cross-slip. Little evidence was found by these workers of any preferential nucleation of the intermediate precipitate along single dislocations. From this and from a study of the effect of sub-grain structure, Holl[26] concluded that the controlling factor for the nucleation of the intermediate precipitate was probably not the vacancy concentration (trapped during the quench from the high temperature) but a critical zone size. Embury and Nicholson[27] maintained, however, that the apparently homogeneous nucleation of precipitates within the grains was largely governed by the concentration and distribution of vacant lattice sites. It should also be pointed out that the last two workers found streaks along the <111> directions in the electron diffraction patterns. These could be attributed to a f.c.c. transition phase analogous to the α' intermediate precipitate in the aluminum-zinc system.

From the above review of the literature it is evident that the process of pre-precipitation in the ternary Al-Zn-Mg alloy system has not been completely explained. The aged structure and the ageing sequence obviously depend on the composition (for example, the Mg:Zn ratio affects the nature of ordering within the zones), and the heat treatment (for example, the ageing temperature may be above or below the upper temperature limit for G-P zone stability). For the present study, therefore, it

seemed worthwhile to investigate the ageing sequence of two alloys of the same Zn but different Mg contents, so that the dependence of the structure on the composition, and its consequent effect on hardening, could be established.

CHAPTER III

EXPERIMENTAL METHODS

Preparation of Specimens

Melting

The metals used for alloy preparation were high purity aluminum obtained from the Reynolds Metals Company, zinc obtained from the American Smelting and Refining Company, and magnesium obtained from the Dow Chemical Company. The lot analyses of the aluminum and zinc are given in Table 1. Lot analysis of the magnesium was not available but the triply-distilled form of the metal used assured at least 99.99 percent purity.

Table 1. Lot Analyses of Aluminum and Zinc

Element	Aluminum (wt. %)	Zinc
Sb		Not detected
Ti		Not detected
Mg	.001	1 ppm
Mn		Not detected
Pb		1 ppm
Sn		Not detected
Si	.001	< 1 ppm
Cr		Not detected
Fe	.001	< 1 ppm
Ni		Not detected
Cu	.002	1 ppm
Al	Balance	Not detected
Ca		Not detected
In		Not detected
Cd		Not detected
Ag		1 ppm
Zn		Balance

Two alloys were prepared by melting the charge in a graphite crucible using an electric resistance furnace. The magnesium was placed in a hole drilled in an aluminum block and the block was placed in the crucible and heated to just above the melting point of aluminum. When this charge was molten the zinc was added. The ingots weighed approximately 250 grams and were about $2\frac{1}{2}$ inches x $1\frac{1}{2}$ inches x 1 inch in size.

The nominal compositions of the two alloys prepared in this manner are given in Table 2A. Chemical analysis by the analytical Chemistry Group of the Oak Ridge National Laboratory gave the final composition, shown in Table 2B.

Table 2A. Nominal Composition of Alloys Examined

	ALLOY 1 (Wt. Percent)	ALLOY 2 (Wt. Percent)
Mg	0.5	1.0
Zn	6.5	6.5
Al	Balance	Balance

Table 2B. Chemical Analyses Composition of Alloys Examined

	ALLOY 1		ALLOY 2	
	Wt. Percent	At Percent	Wt. Percent	At Percent
Mg	0.51	0.72	0.71	1.09
Zn	5.77	2.46	5.82	2.47
Al	Balance	Balance	Balance	Balance

Heat Treatment

Homogenization. The as-cast ingot was cut into 3/4 inch x 1 inch x $1\frac{1}{2}$ inch plate and these plates were soaked at 200°C for a period of two weeks to eliminate the low melting point eutectics. Following this preliminary homogenization the as-cast structure which persisted was broken down by a controlled schedule of rolling and intermediate annealing treatments. The cross-sectional area was thus reduced 50 percent and the final homogenization was accomplished by holding the plates at 500°C for one week. Photomicrographs of the two alloys in the as-cast condition and after homogenization treatment are shown in Figures 4(a) and 4(b) and Figures 5(a) and 5(b), respectively.

Age-hardening Heat Treatment. This consists of solution heat treatment, quenching, and subsequent ageing at some low temperature. The solution heat treatment was carried out in a tube furnace with a uniform temperature zone of about 2 inches. The temperature for attaining the single-phase structure was chosen based on considerations of maximum uniformity of structure (i.e., complete recrystallization) and a minimum, or at least a constant precipitate-free zone width next to the grain boundary. It has been found by Taylor[30] and Murakami, et al[31] that the solution treatment is best carried out above 440°C, and particularly at 460°C. It is seen from the phase diagram in Figure 3 that at this temperature both alloys are well within the single-phase region.

An iced brine quench was used for all hardness samples. For the x-ray and electron microscopy foil specimens a direct quench into water at 20°C was employed. The x-ray powder filings for x-ray diffraction were quenched into iced brine bath in their pyrex capsule. The tube imploded

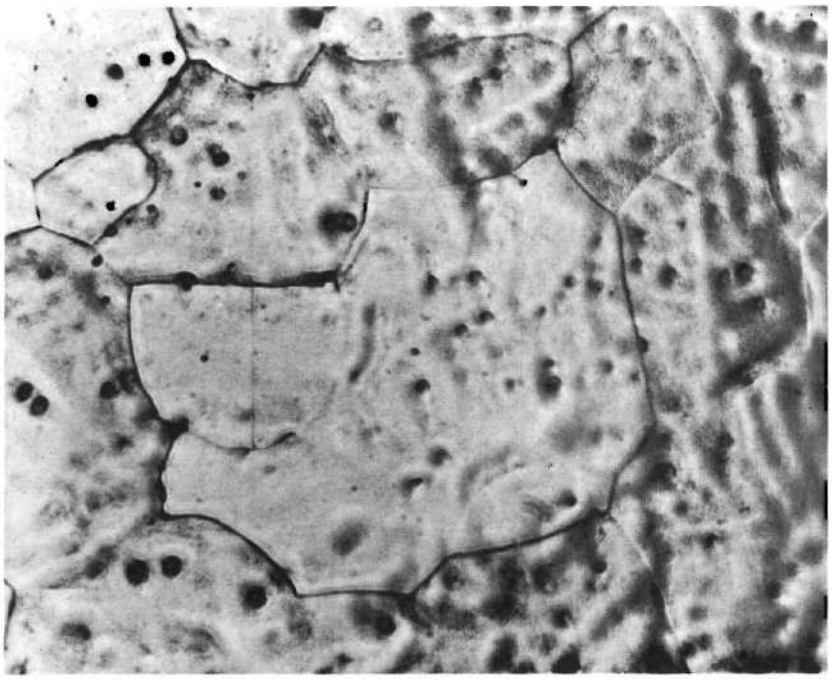

Figure 4(a). Photomicrograph of As-cast Al, 2.46 At. Percent Zn, 0.72 At. Percent Mg Alloy (Magnification 140 X).

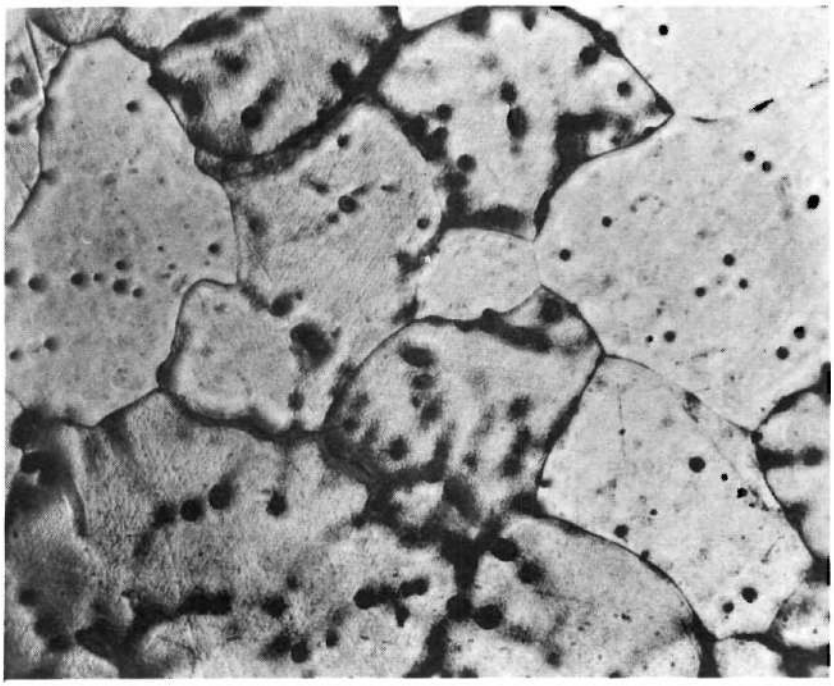

Figure 4(b). Photomicrograph of As-cast Al, 2.47 At. Percent Zn, 1.09 At. Percent Mg Alloy (Magnification 140 X).

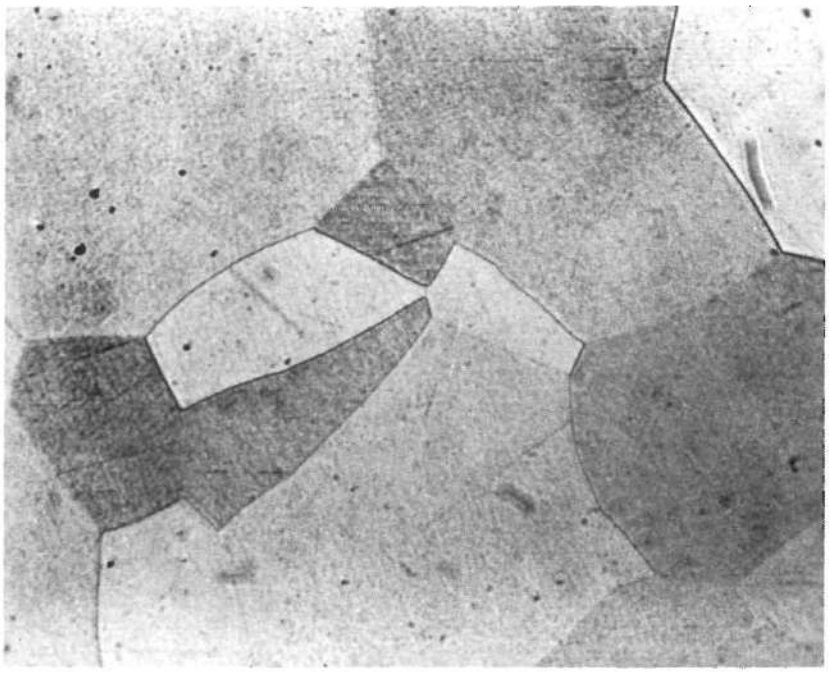

Figure 5(a). Photomicrograph of Homogenized Al, 2.46 At. Percent Zn, 0.72 At. Percent Mg Alloy (Magnification 140 X).

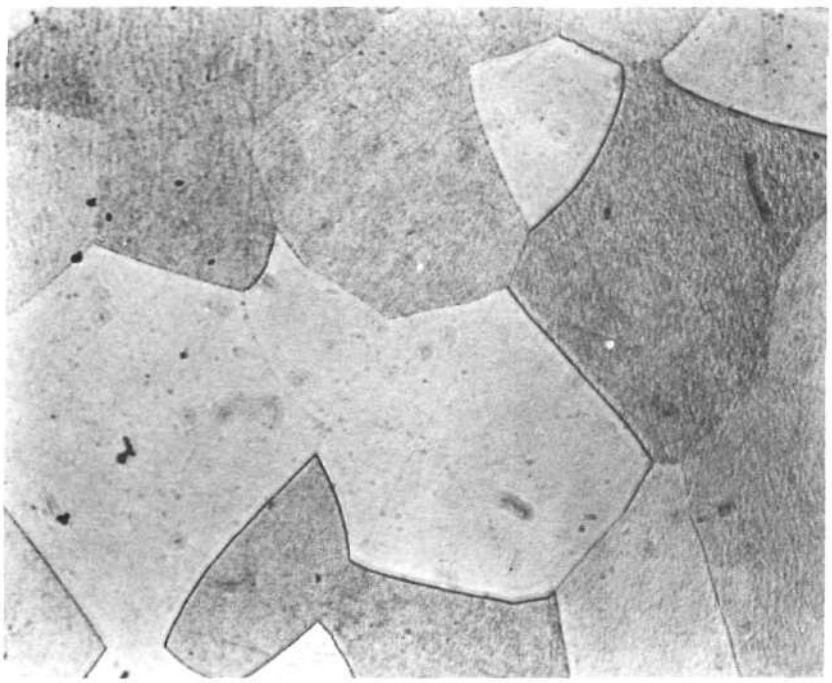

Figure 5(b). Photomicrograph of Homogenized Al, 2.47 At. Percent Zn, 1.09 At. Percent Mg Alloy (Magnification 140 X).

due to the thermal shock and thus a rapid quench was obtained.

Three temperatures were chosen for ageing. These were 50°, 75°, and 135°C, all three being below the upper temperature limit for the G-P zone stability as determined by Polmear[10]. Ageing was carried out in oil baths controlled to ± 1°C. The foil samples for the isothermal small-angle scattering studies were aged in the camera in a special sample holder described elsewhere[32]. Photomicrographs of the two alloys, aged to maximum hardness are shown in Figures 6(a) and 6(b).

Foil and Powder Preparation

For small-angle x-ray studies and for transmission electron microscopy thin metal foils were needed. These were obtained by alternate cold-rolling, between two strips of stainless steel, and annealing treatments. The optimum thickness for transmission x-ray studies is $1/\mu$, where μ is the absorption coefficient of the sample for the radiation used. For the alloys under study this was approximately 0.07 mm. All the foils were degreased by washing in ethanol before being subjected to any heat treatment. Foils for the electron microscopy study were obtained by electropolishing the suitably heat-treated material. The high temperature of stress-relieving and solution treatment resulted in the formation of a passive oxide film on the surface of the foil. It was thus necessary to remove this, prior to electropolishing, by chemically polishing in a solution of 5 percent HNO_3, 25 percent H_2SO_4, and 70 percent Orthophosphoric acid, and then rinsing in water.

The method used for electropolishing was a modification of the methods of Glenn and Raley[37], and Nicholson, Thomas, and Nutting[29]. An electrolyte of 1:4 HNO_3 in CH_3OH was used in conjunction with a stainless

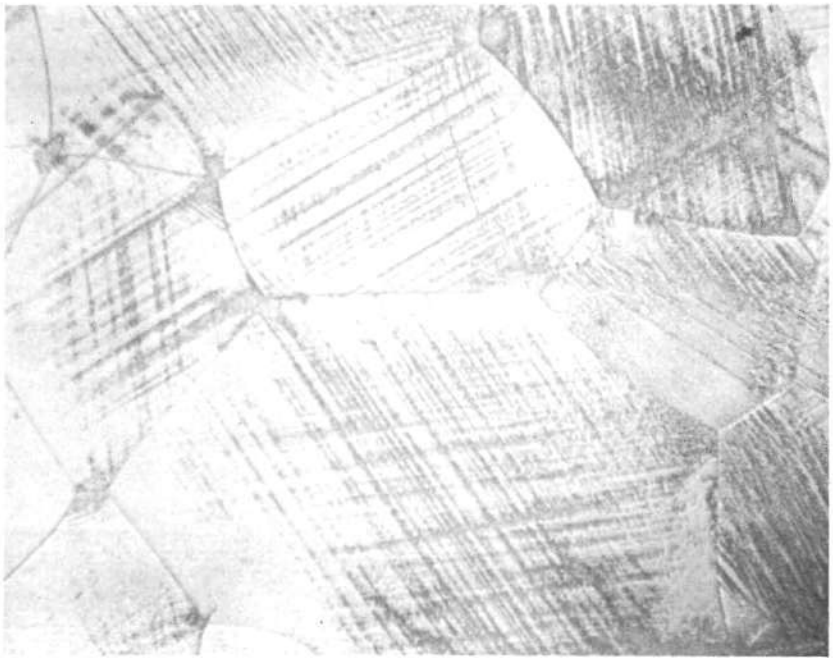

Figure 6(a). Photomicrograph of Al, 2.46 At. Percent Zn, 0.72 At. Percent Mg Alloy Solution Treated at 460°C and Aged at 135°C to Maximum Hardness (Magnification 100 X).

Figure 6(b). Photomicrograph of Al, 2.47 At. Percent Zn, 1.09 At. Percent Mg Alloy Solution Treated at 460°C and Aged at 135°C to Maximum Hardness (Magnification 100 X).

steel cathode and with the sample serving as the anode. The edges of the foil were coated with lacquer to prevent any preferential polishing of these areas. The temperature for sufficiently slow electropolishing was found to be critical and was maintained below -45°C by immersing the cell in a bath of dry ice and acetone. Under these conditions thinning occurred uniformly with a voltage of about 10 volts.

Fine powder required for the x-ray powder diffraction patterns was obtained by filing a homogenized plate using a fine jeweler's file. The filings were magnetically separated from iron filings and were then sieved through a 200-mesh nylon screen.

Examination of Specimens

Metallography

The representative samples to be studied metallographically were mounted in "Quickmount" self-setting resin. The samples were ground flat and the flat surface was polished through 600 grit silicon carbide paper, followed by rough wheel polishing through 0.3 μ aluminum oxide. The final polishing was accomplished by polishing on "microcloth" using heavy magnesium oxide suspended in distilled water as abrasive. In all cases an aluminum polishing wheel was used to prevent possible electro-corrosion due to a wheel less electro-negative than the samples. All the specimens were inspected under the microscope in the as-polished condition and no abnormalities were observed. The specimens were etched lightly with dilute Keller's solution (1 percent HF, 1.5 percent HCl, 2.5 percent HNO_3, and 95 percent H_2O), given a microcloth polish, and re-etched for observation.

Hardness Measurements

The hardness of polished samples, after quenching and ageing for various lengths of time, was obtained by using a Vickers tester. Generally one hardness sample was used for a particular temperature and three readings were taken on each occasion. Five and 10 Kgm loads were employed for the testing.

X-ray Measurements

Small-angle Measurements. The diffracted intensity in the range 0.25° to 4° (angles in 2θ) was measured with counter techniques, using a Kratky camera. A schematic illustration of the small-angle scattering apparatus used is given in Figure 7.

In order to understand the geometry, consider first Figure 8, which shows an early design of a small-angle scattering device. The first pair of apertures, S_1 and S_2, normal to the plane of the figure, have an opening of the order of 0.1 mm, and they define the incoming beam. The third slit, S_3, eliminates scattering due to the edges of S_2. With this arrangement it is not possible, however, to study the scattered intensity in the region Z. This shortcoming was eliminated in the device described by Kratky[34] and shown in Figure 9. The horizontal surface of the blocks B_2 and B_3 are normal to the plane of the figure. The primary beam is initially defined by the slit formed by B_1 and B_2 edges. The extended plane face of B_2 and the lower face of B_3 further limits the beam. Thus, no undesired diffraction occurs above the line H. As seen in Figure 9 this is easily realized in the present apparatus.

In the present study Ni filtered Cu radiation at 30 mA, 40 Kv was used for all the specimens. Two pairs of entrance and exit slits were

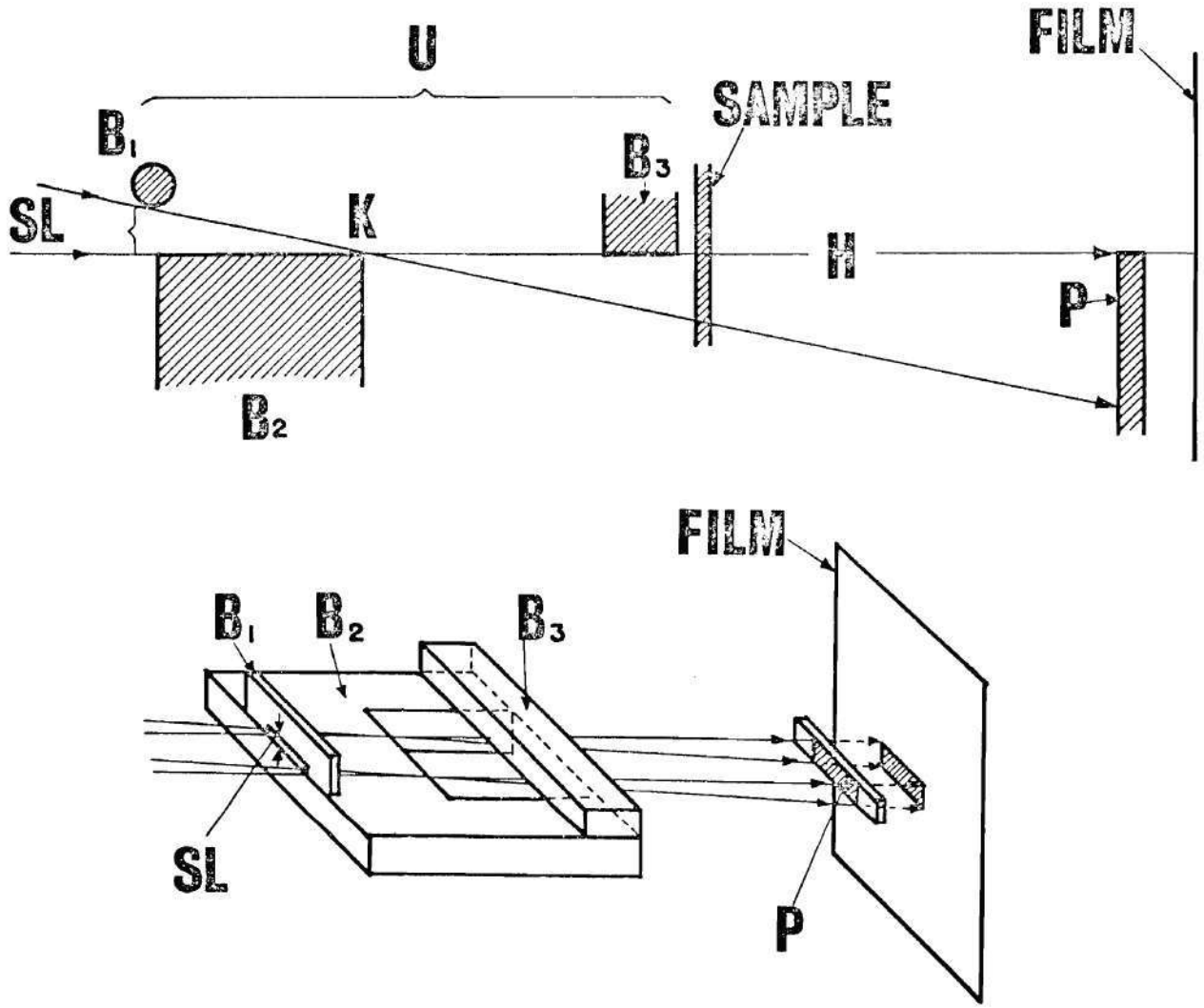

Figure 7. Schematic of a Small-angle Scattering Set-up.

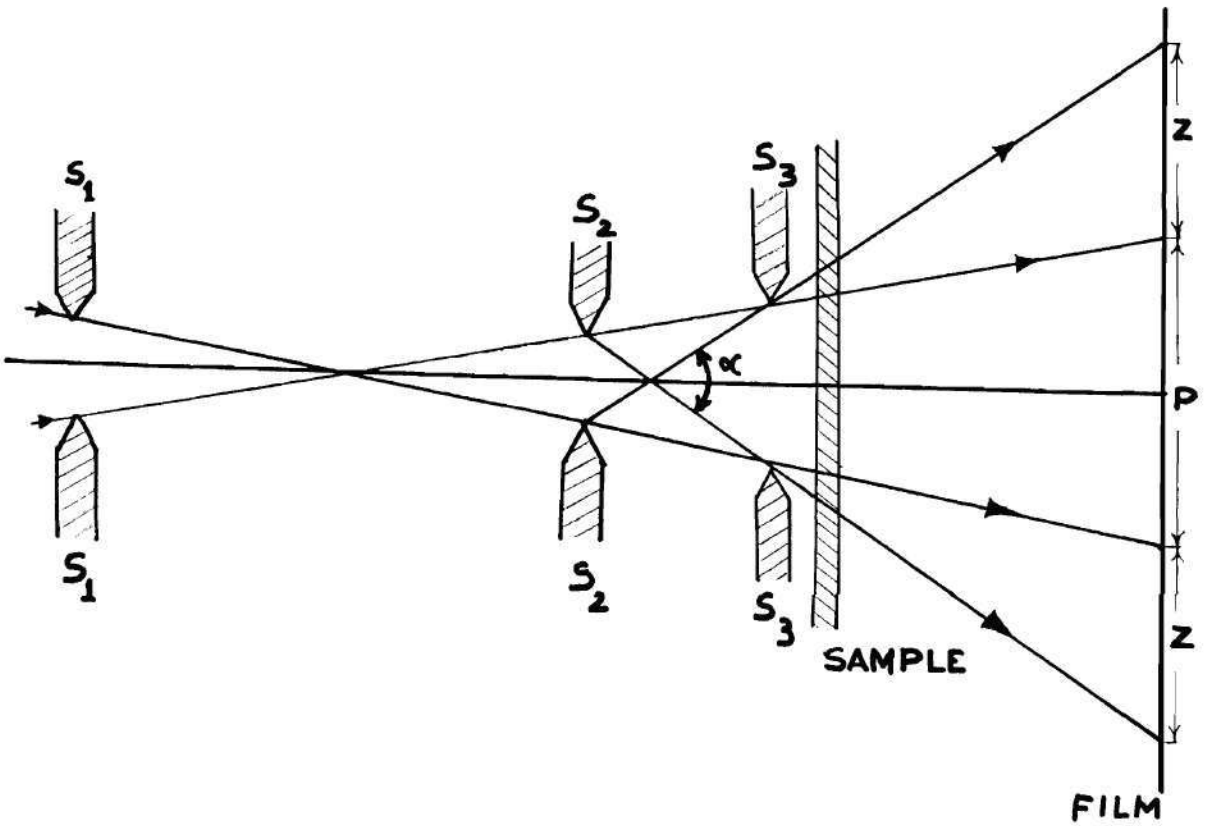

Figure 8. An Early Design of a Small-angle Scattering Camera.

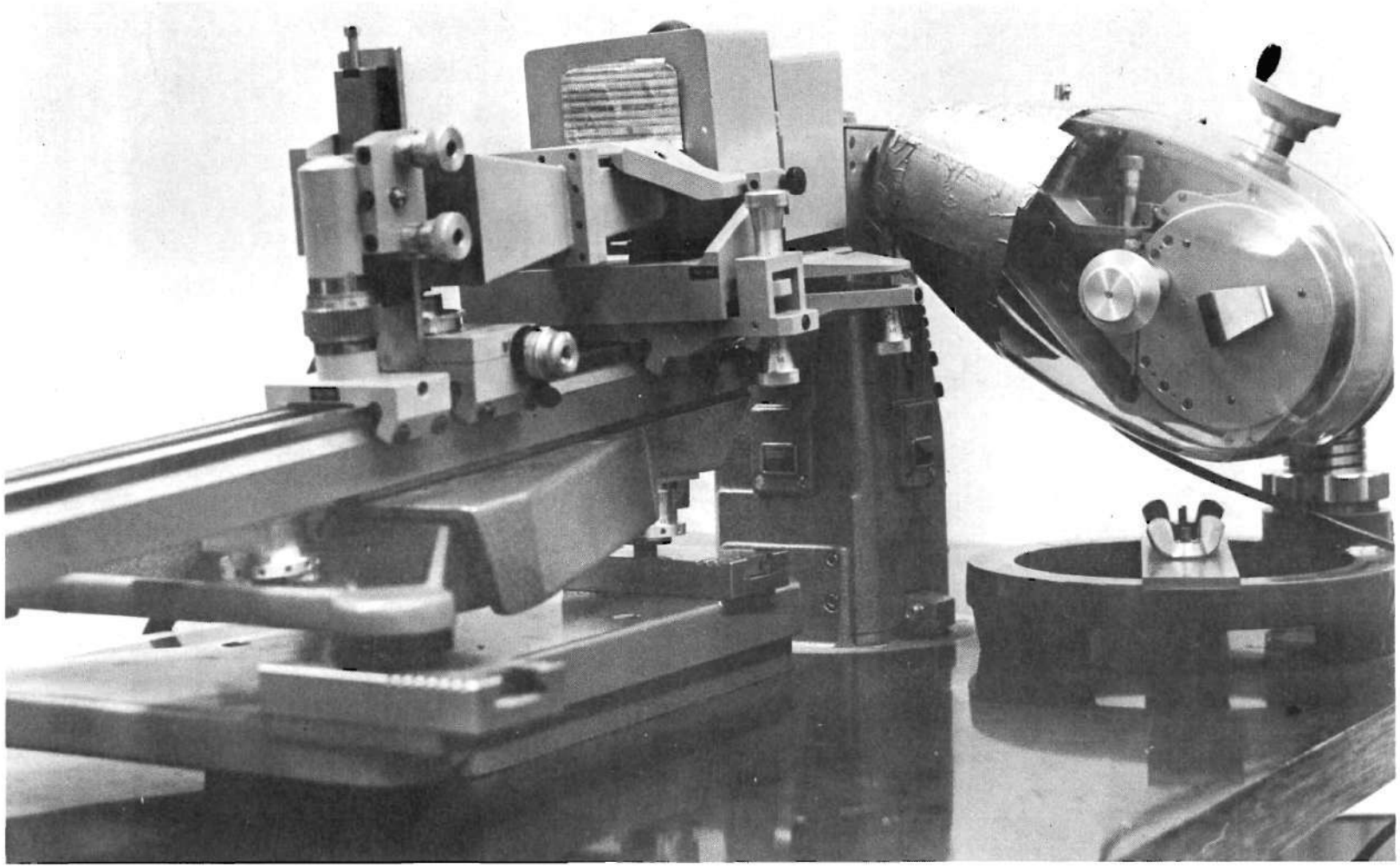

Figure 9. A Kratky Small-angle Scattering Camera Set-up for Photographic Recording. The Guinier de-Wolff Focussing Camera Used for Powder Diffraction Studies is Shown.

employed and the centroid of the beam in each case was determined to mark the zero scattering angle ($2\theta = 0^{o}$). These were:

(a) Entrance slit - 101 μ

Exit slit - 400 μ

Centroid of primary beam (elevation) - 2146.9 μ

(b) Entrance slit - 60 μ

Exit slit - 200 μ

Centroid of primary beam (elevation) - 2297 μ

The centroid of the beam was determined by obtaining the beam profile using a 50 μ exit slit. The background, determined by using a pure Al foil 0.021 inches thick and having an attenuation factor (T) = 0.33768, was used to correct the small-angle scattered intensity at all elevations.

Solution treated and aged foils of both alloys were cooled by passing air through a copper coil immersed in liquid nitrogen. Step scanning was effected at intervals of 200 μ with a fixed time of 100 seconds, up to an elevation of 6800 μ. The step scanning interval was changed, thereafter, to 1000 μ up to a maximum of 16200 μ.

The continuous isothermal ageing studies of the foils were made at two temperatures, 75°C and 135°C. The ageing of the foils was carried out in the sample holder referred to earlier and the change in the scattered intensity was followed at a fixed elevation of 4357 μ (corresponding to 0.0103 radians).

The scattered intensity obtained was corrected for background and then converted to give relative absolute intensity. This was done by comparing each measured intensity with the intensity scattered by a Lupolen standard at an angle corresponding to a Bragg value of 150 Å. The Lupolen

used had previously been calibrated by O. Kratky. Use was then made of the following relation:

$$I_o = 1/92.2 \left[(\text{counts/sec.})_{\text{Lup, } 150\ \text{Å}} \times a \times T_{\text{sample}}/F \right].$$

I_o then represents the intensity of the primary beam weakened by the scattering sample. In the above, a is the distance between the sample and the plane of registration, and F is the detector slit area. The constant 92.2 contains the attenuation factor for the Lupolen standard. By normalizing the scattered intensity (I) at each elevation by I_o, the relative absolute intensity is then obtained. A detailed discussion of the theory of SAS is given in Appendix A.

Measurements above $2\theta = 10^\circ$. A General Electric XRD-6 diffractometer was used to measure the diffuse scattering for the angular range between $2\theta = 10^\circ$ to $2\theta = 28^\circ$. The Warren doubly-bent monochromator[36] was used and the experimental arrangement is shown in Figure 10. Since diffuse intensities were being studied, air scattering was eliminated by evacuating the column around the specimen. CuK_α radiation at 35 kV and 20 mA was used. Balanced Ni and Co filters were employed in the primary beam to eliminate extraneous radiation and fluorescence due to $\lambda/2$ wavelength. Pulse height discrimination was also applied in conjunction with a proportional counter. The baseline voltage was 1.8 volts and the window was 2 volts. A 0.2° receiving slit was used in all cases. An accumulated count of 10,000 counts was allowed for the Ni filter. The average time taken for this count was then the fixed time for counting with the Co filter in the beam.

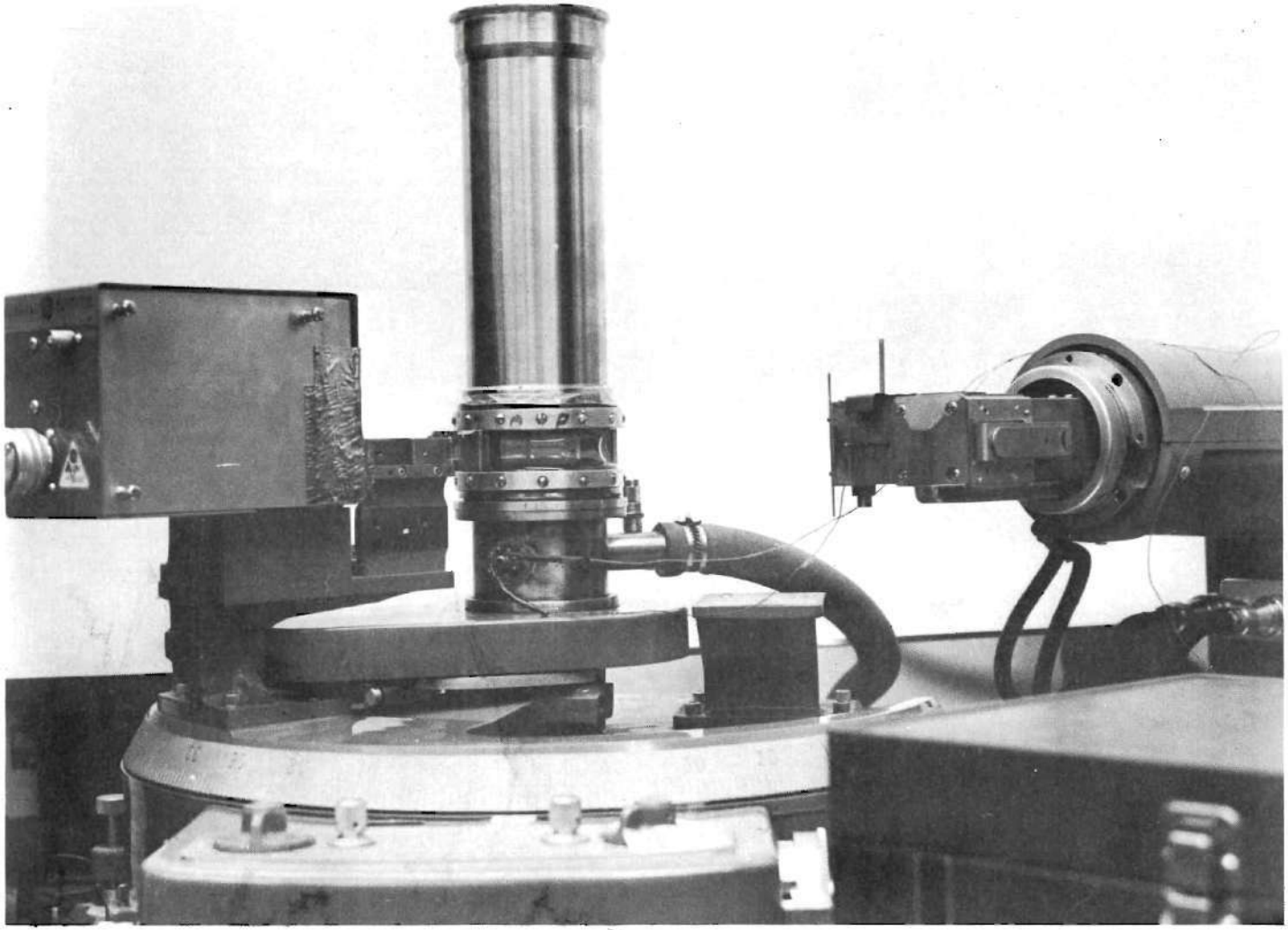

Figure 10. The General-Electric X-ray Diffractometer Used in the Present Research.

Since the time required for the step scanning was fairly large, it was necessary to minimize the changes during the period of study. This was done by cooling the specimen to a temperature of -40°C by means of a cryostat. Thus, thermal diffuse scattering was also minimized.

Powder Diffraction Patterns. Powder diffraction patterns were obtained on a Nonius-Guinier de Wolff focussing camera. The principle of the geometry is the well-known Guinier type focussing. A bent crystal reflects K_α radiation from the target into a sharp focal line. This is a Bragg reflection; therefore each ray converging to the focal line is the reflection by the crystal planes of a single, well defined ray in the primary beam from the target. The crystal is a quartz slab cut at an angle of $4\frac{1}{2}^\circ$ with the (101) planes. It is bent in a slightly asymmetric way so as to approximate a logarithmic spiral, the center of which is at the focal point.

Figure 9 shows the Guinier camera as used in the present investigation, i.e., in the vertical position. The x-ray tube was operated at 50 kV and 20 mA. By evacuating the camera it was possible to reduce the background greatly. Under these conditions it was possible to obtain the diffraction lines due to extremely weak reflections.

Electron Microscopy

The electron microscopy observations were made of thin foils of the two alloys using a Phillips EM 200 electron microscope, with a metallurgical stage. As the foils oxidize rapidly it was found necessary to use a liquid nitrogen decontaminating device (referred to as the cold finger).

In summary, the methods used in the present investigation were: metallography, electron microscopy, powder diffraction, diffuse and small-

angle x-ray investigations for structure studies, and hardness measurements to follow changes in mechanical properties.

CHAPTER IV

RESULTS

The ageing sequence in two ternary Al-Zn-Mg alloys has been studied in terms of their structure and strength. The choice of two compositions, Al, 5.82 weight percent (2.47 at percent) Zn, 0.71 weight percent (1.09 at percent) Mg, and Al, 5.77 weight percent (2.46 at percent) Zn, 0.51 weight percent (0.72 at percent) Mg, permitted a study of the effect of Mg:Zn ratio on the ageing phenomenon in these alloys. Hardness measurements provided an indication of the strength as well as the progress of ageing and was thus used to select the ageing times and temperatures for x-ray investigation. Powder diffraction methods and diffuse x-ray investigations were undertaken to obtain detailed information on the nature of the structure responsible for the hardening while small-angle scattering studies were used for quantitative analysis of the size and volume fraction of the G-P zones at various stages of ageing.

Hardness - Time Results

The hardness of the two alloys was determined as a function of ageing time and ageing temperature. Figures 11, 12, and 13 show the hardness versus logarithm of time plot of these measurements for the magnesium-poor (0.72 atomic percent) alloy aged at 50°, 75°, and 135°C. For the 50°C ageing, it is observed that only linear hardening occurs over the entire period of examination. Ageing at 75°C also produces no overageing. Upon ageing at 135°C, however, the pattern of hardening changes and appears to

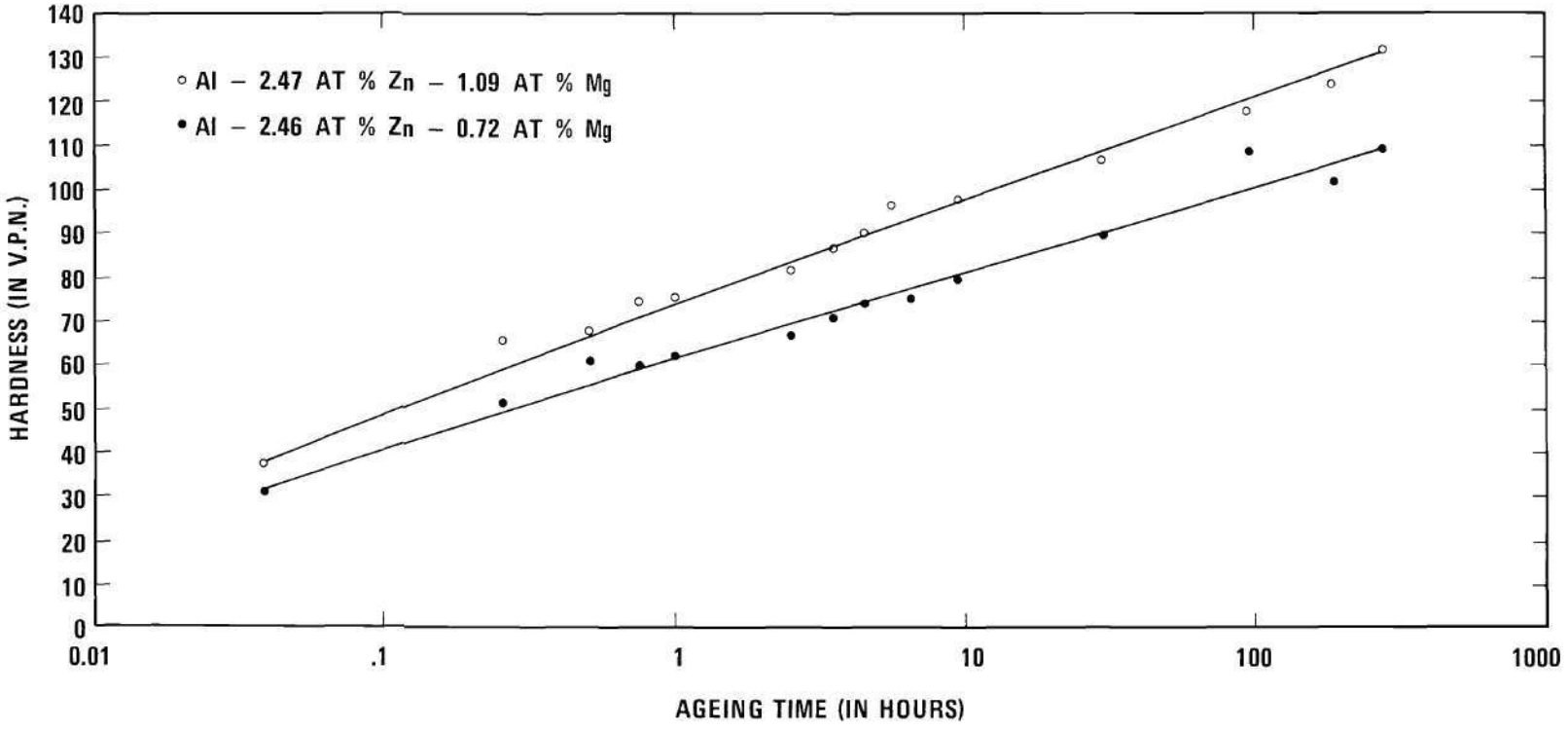

Figure 11. Results of Hardness Measurements Upon Ageing at 50°C.

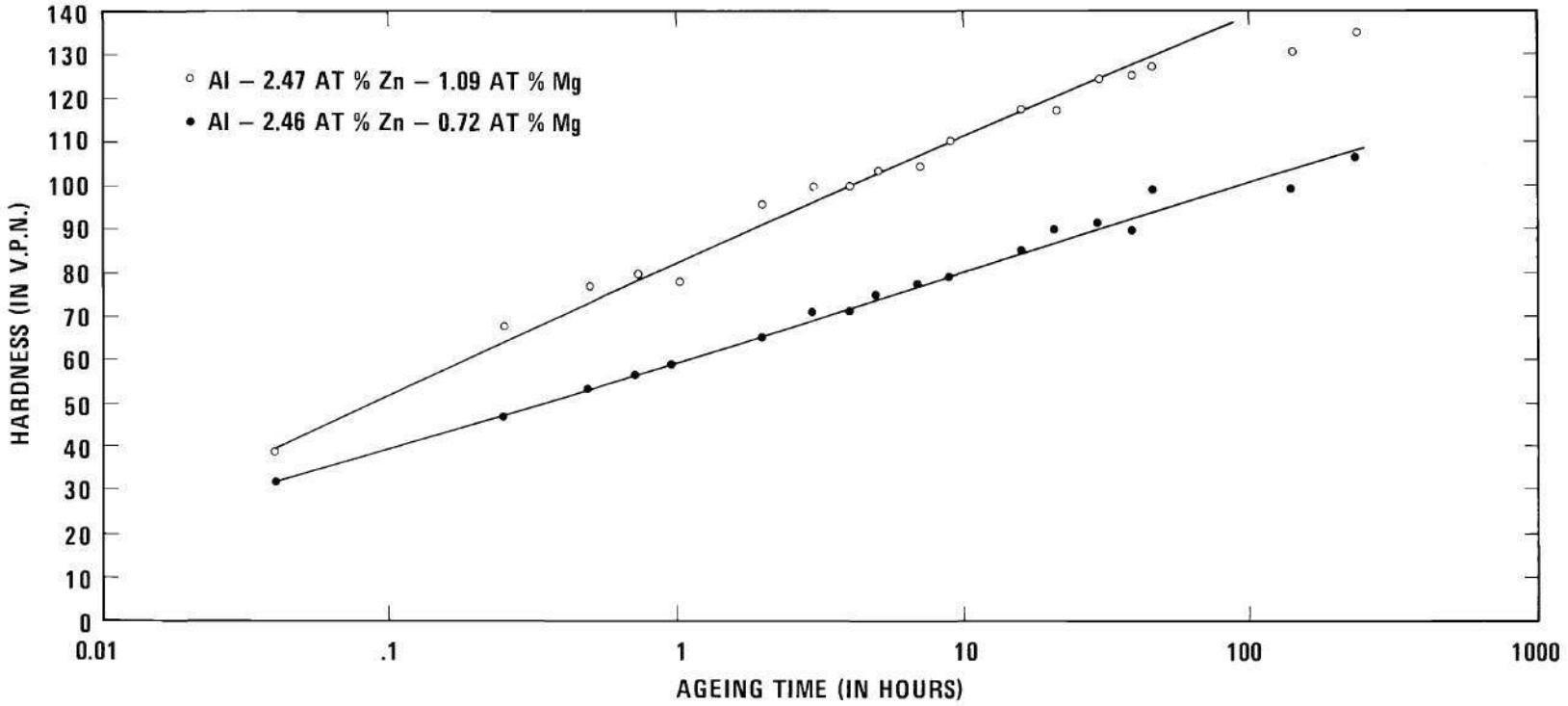

Figure 12. Results of Hardness Measurements Upon Ageing at 75°C.

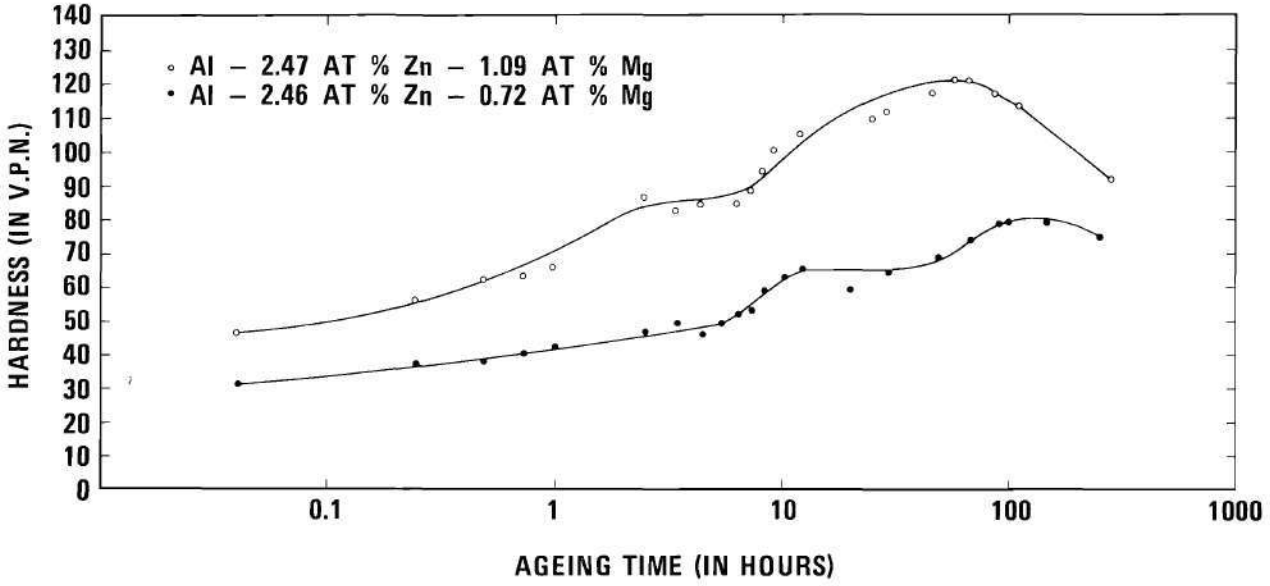

Figure 13. Results of Hardness Measurements Upon Ageing at 135°C.

occur through a series of stages. Thus, from an as-quenched hardness of 30 Vickers Pyramidal Number (VPN), hardness increases linearly up to 48 VPN in about 6 hours; this is followed by a period of accelerated hardening during which the hardness increases very rapidly. This lasts for about 5 hours. The hardness then levels out until about 35 hours of ageing, after which the hardness increases rapidly again to a peak hardness of 70 VPN. Overageing is seen to result after 110 hours.

The figures also show the variation of the hardness with time for the magnesium-rich (1.09 atomic percent) alloy for the three ageing temperatures used. As in the previous case, linear hardening without overageing is observed only when this alloy is aged at either 50° or 75°C. Again the nature of the ageing process changes for ageing at 135°C and it is seen that a two-stage hardening sequence is exhibited in this case. A linear increase in hardness from 40 VPN to 86 VPN occurs in the first $2\frac{1}{2}$ hours, followed by a period of constant hardness. Rapid hardening occurs immediately thereafter but after this the hardness continues to increase at a diminishing rate until a peak hardness of 120 VPN is attained after 60 hours of ageing.

Small-angle Scattering Results

The results of the small-angle scattering experiments on the magnesium-poor alloy are shown in Figure 14, which is a plot of the relative absolute diffracted intensity versus 2θ. The scattering from the alloy, after the solution-heat treatment and in the as-quenched condition is seen to be negligible. Small-angle scattered intensity is found to increase with progressive ageing and appears to get concentrated in a narrower re-

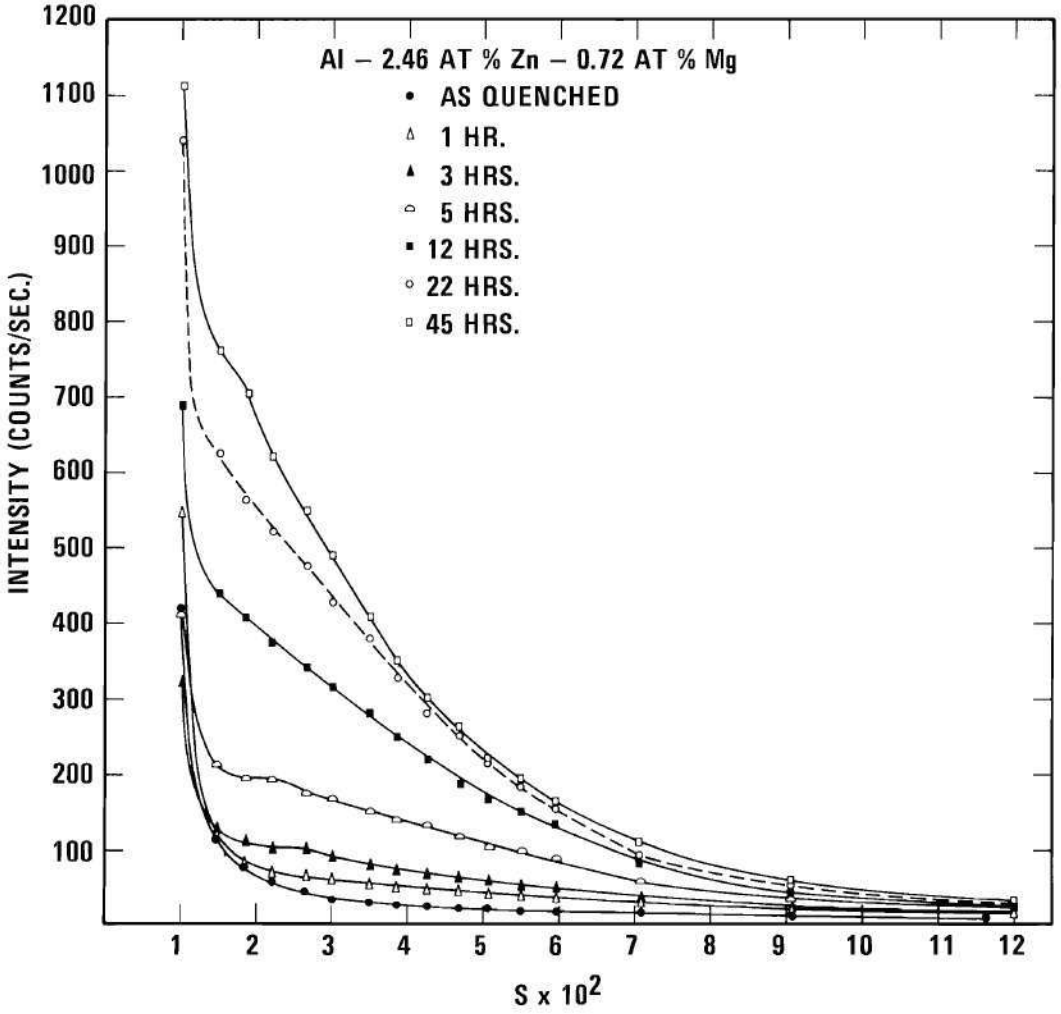

Figure 14. X-ray Small-angle Scattering Results for Al, 2.46 At. Percent Zn, 0.72 At. Percent Mg Aged at 135°V.

gion about the primary beam. Figure 16 shows the variation of the normalized integrated intensity with time at 135°C. A steady increase of the integrated intensity occurs in the initial stages but at the later stages the intensity increases rapidly. This anomalous increase in the integrated intensity takes place when the intermediate precipitate is thought to appear and hence is attributed to particle size effects of this phase. The results of the isothermal ageing treatments for this alloy are shown in Figures 17 and 18 for the two ageing temperatures 75° and 135°C.

The results of similar experiments on the magnesium-rich alloy are given in Figures 15 through 18.

The size of the zones at various stages of ageing were obtained by using the Guinier approximation[38] of the scattered intensity, utilizing the slope of a logarithm of scattered intensity versus ϵ^2 (ϵ is the scattering angle) plot. The results of such an analysis are given in Table 3. The variation of the zone radius upon ageing at 135°C for the two alloys is shown in Figure 19.

Powder Diffraction Patterns

Table 4 shows the d values greater than 2 Å, which appear in the powder diffraction patterns for specimens of the two alloys aged for various times at 135°C. Also tabulated are the spacings of the terminal solid-solution of aluminum, $MgZn_2$, MgZn, and Al_2O_3. The diffraction lines for d values greater than 3 Å were obtained using the diffractometer and plate specimens; this was necessary because of the extremely diffuse nature of the lines in the powder patterns. The effect of preferred orientation was negligible on the low-angle diffuse lines.

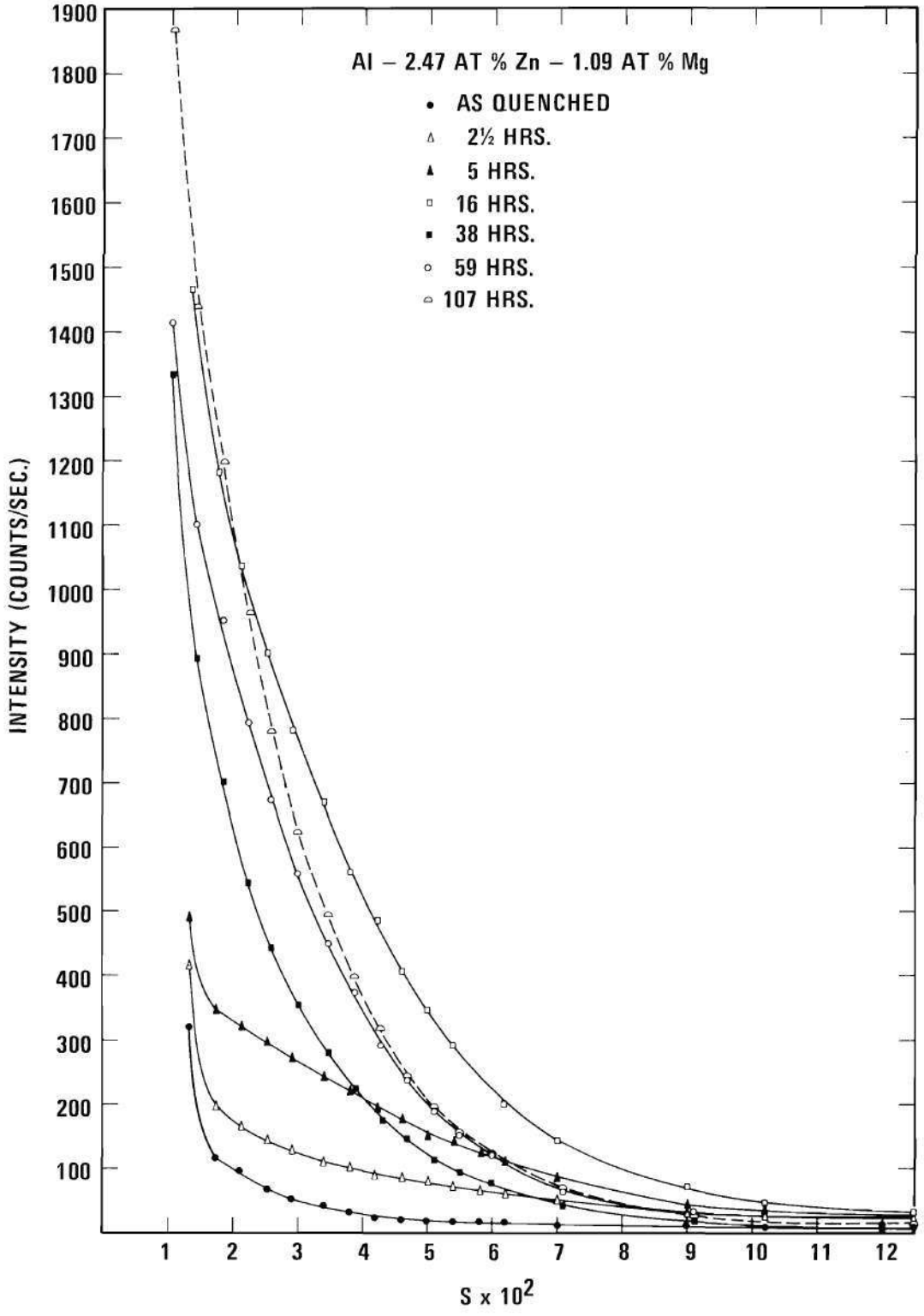

Figure 15. X-ray Small-angle Scattering Results for Al, 2.47 At. Percent Zn, 1.09 At. Percnet Mg Aged at 135°C.

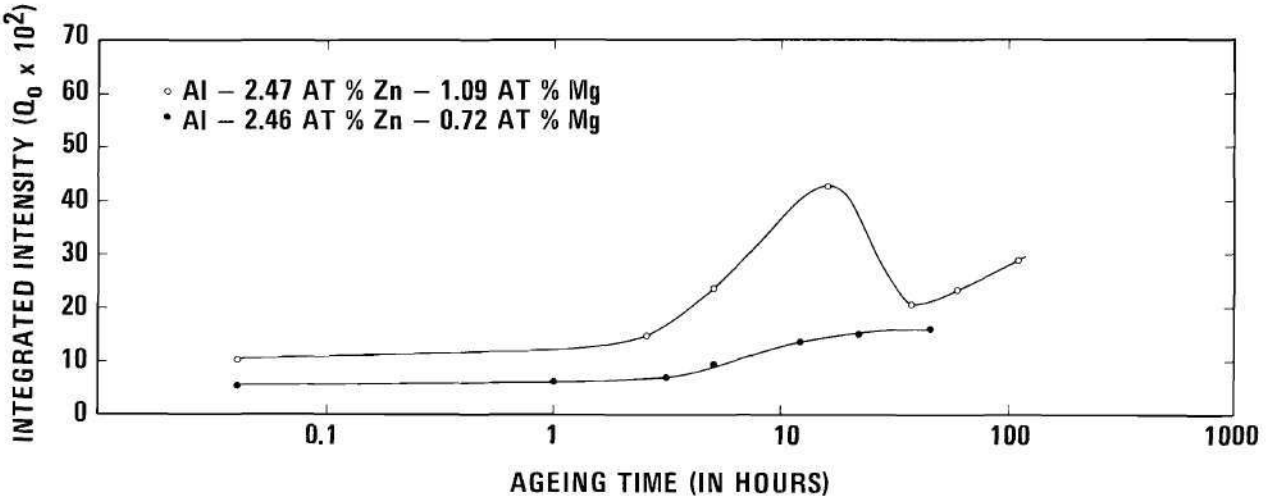

Figure 16. The Variation of Integrated Intensity with Time Upon Ageing at 135°C.

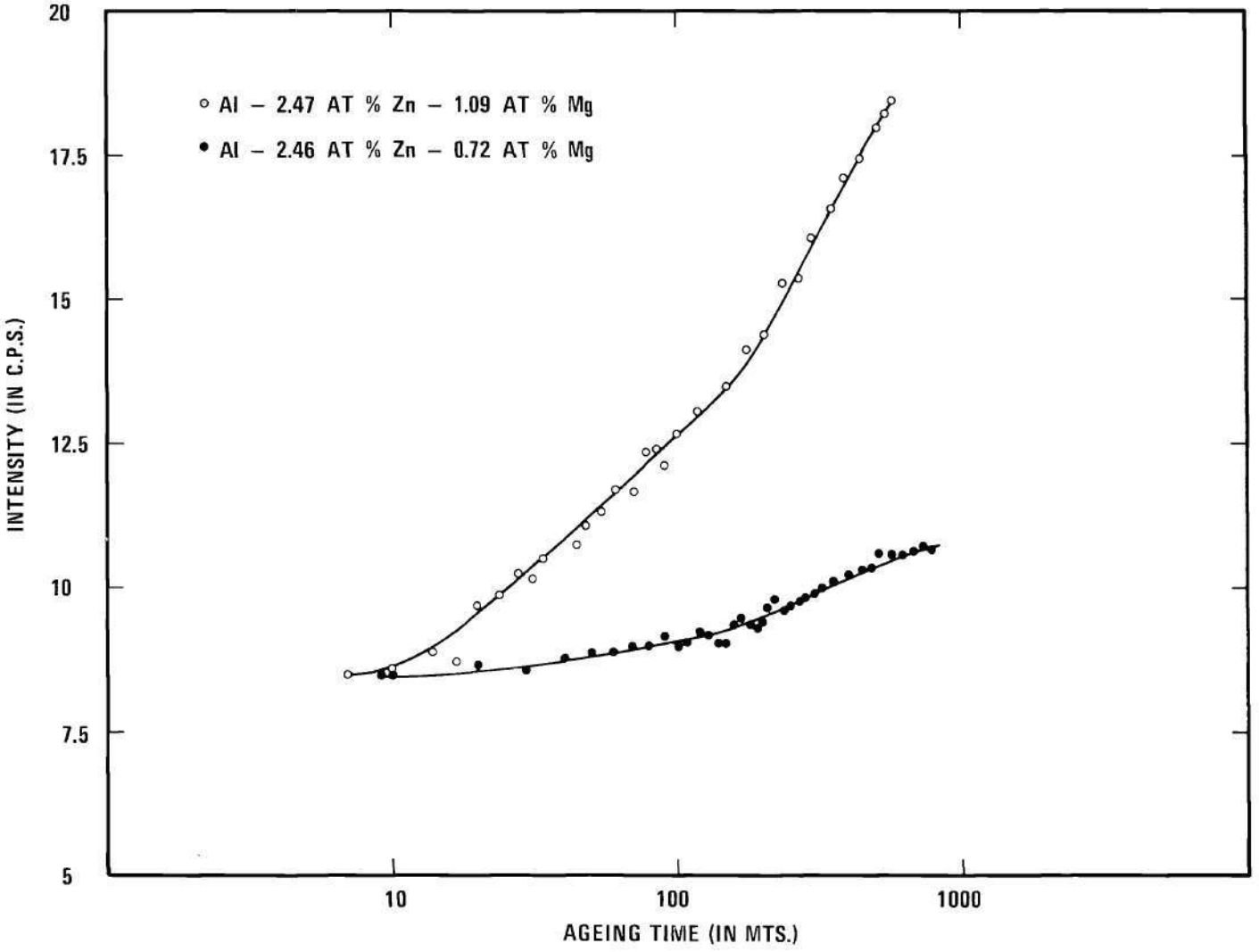

Figure 17. X-ray Small-angle Scattering at 2θ = 0.0103 Radians Upon Isothermal Ageing at 75°C.

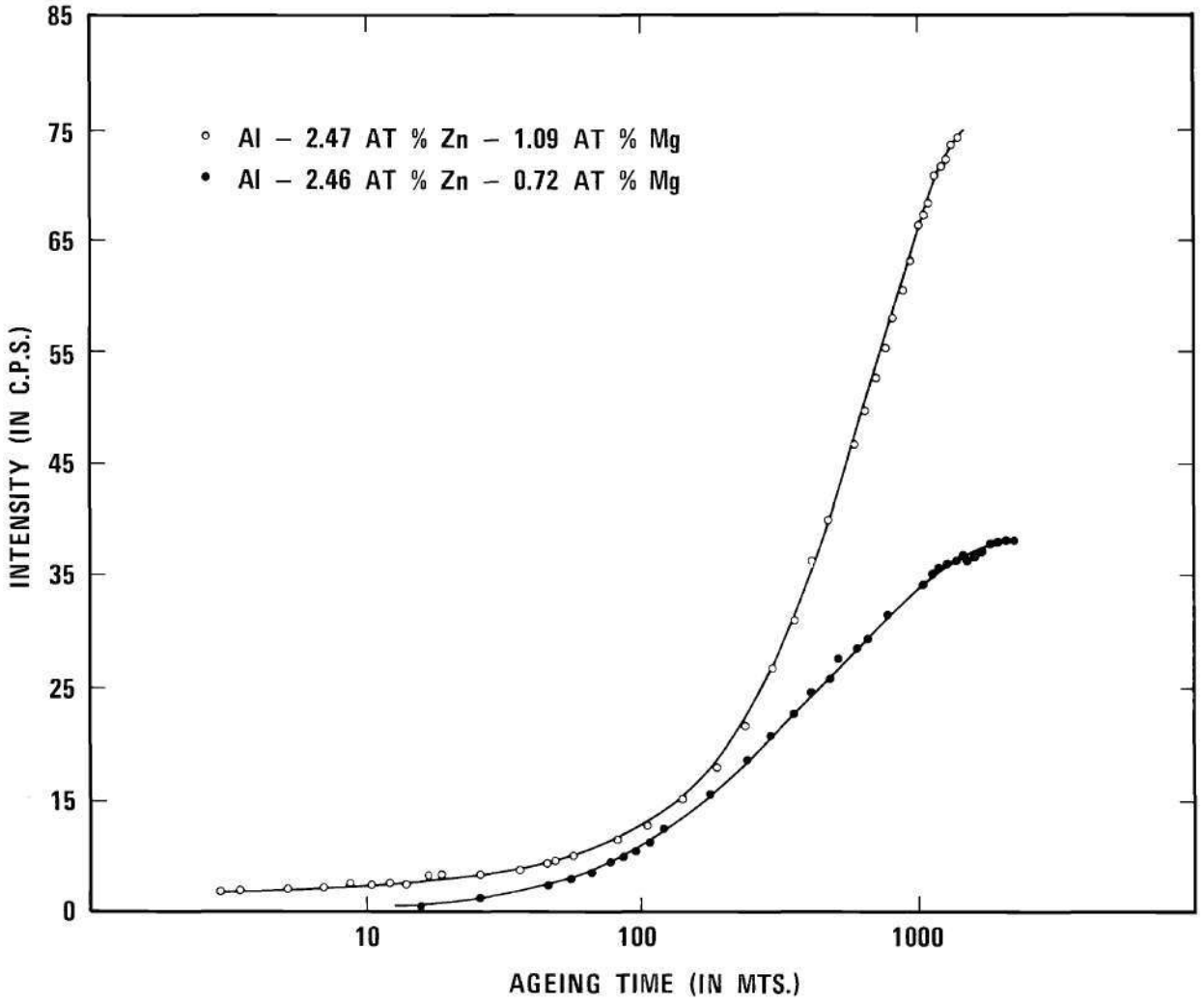

Figure 18. X-ray Small-angle Scattering at $2\theta = 0.0103$ Radians Upon Isothermal Ageing at 135°C.

Table 3. Results of the Calculated Zone Radius and Integrated Intensity

	Al, 2.46% Zn, 0.72% Mg		Al, 2.47% Zn, 1.09% Mg	
Ageing Time (in hours)	R_G(in Å)	$k \int_0^\infty s\,E(s)\,ds \times 10^2$	R_G(in Å)	$k \int_0^\infty s\,E(s)\,ds \times 10^2$
As quenched	13.45	5.9	13.91	10.4
1	18.01	6.3		
$2\frac{1}{2}$			30.75	14.9
3	25.17	6.9		
5	30.3	9.7	35.16	23.5
12	42.13	13.4		
16			45.35	43.3
22	43.3	15.1		
38			49.6	20.5
45	45.5	16.0		
59			53.5	23.2
$107\frac{1}{2}$			58.7	28.7

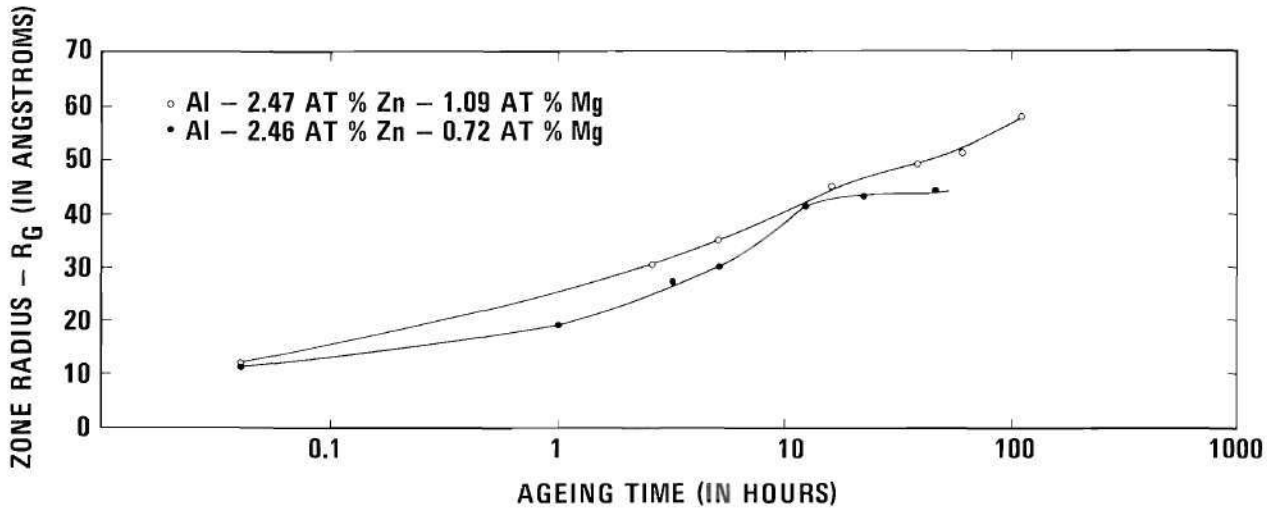

Figure 19. The Variation of Zone Radius with Time Upon Ageing at 135°C.

Table 4. Summary of d Values (A) for Powder Specimens, α Al, (Al_2O_3), MgZn, $MgZn_2$

Al	Al_2O_3	MgZn	$MgZn_2$	Al, 2.46% Zn, 0.72% Mg					Al, 2.47% Zn, 1.09% Mg			
				As Quenched	2½ Hrs. 135°C	38 Hrs. 135°C	110 Hrs. 135°C	4 Weeks 135°C	As Quenched	38 Hrs. 135°C	60 Hrs. 135°C	4 Weeks 135°C
							6.8 DB	6.5 DB		6.8 DB	6.5 DB	6.5 DB
		6.041									5.9 DB	
		5.02										
			4.46			4.67	4.67	4.67	4.667	4.667	4.667	
		4.26	4.20		4.3							
		4.04	3.95		4.15							
		3.61			4.04		4.04	4.04	4.04	4.04	4.04	4.04
						3.3 DB	3.3 DB	3.3 DB	3.9	3.3 DB	3.3 DB	3.3 DB
	2.55		2.58	2.85	2.85	2.85	2.85	2.85	2.85	2.85	2.85	2.85
		2.4	2.4		2.44	2.44	2.44	2.44	2.44	2.44	2.44	2.44
2.34				2.33	2.33	2.33	2.33	2.33	2.33	2.33	2.33	2.33
		2.23	2.2									
	2.08		2.1	2.08	2.08	2.08	2.08	2.08	2.08	2.08	2.08	2.08
2.03			2.02	2.02	2.03	2.03	2.03	2.03	2.02	2.02	2.02	2.02

DB = Diffuse Band

Electron Microscopy

Electron microscopy was restricted to studies of the alloys aged to maximum hardness. The precipitate size determined by microscopy seems to compare well with those obtained by small-angle scattering. Figure 20 is an electron micrograph of a fully aged magnesium-poor alloy. An electron micrograph for a similarly aged magnesium-rich alloy is shown in Figure 21. There was ample evidence of preferential precipitation on dislocations similar to the observations of Nicholson, Thomas, and Nutting[29]. An electron micrograph of such a dislocation decoration is shown in Figure 22. Formation of coarse precipitates at the grain boundaries, which is another preferred site for precipitation, was also observed and is seen in Figure 23.

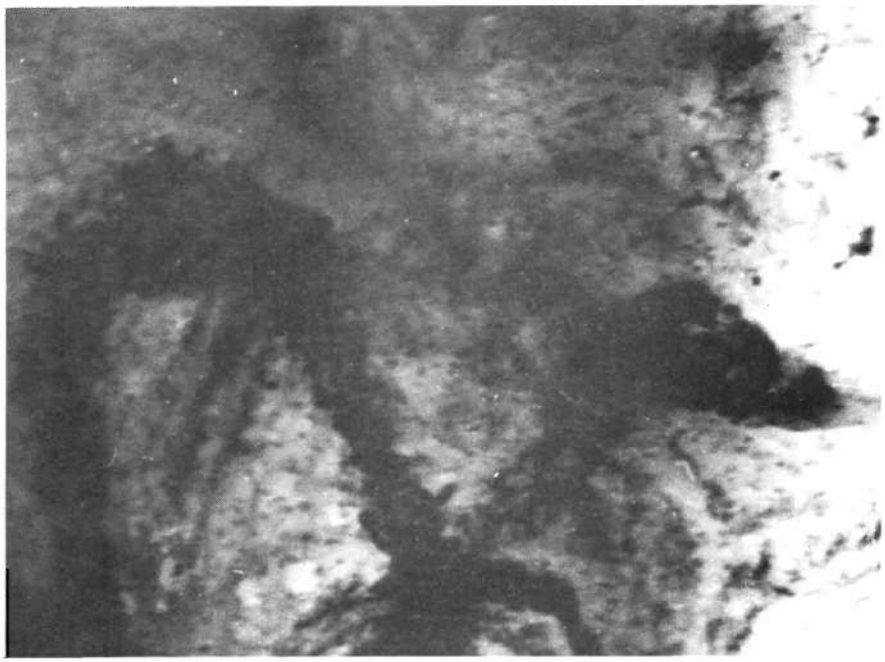

Figure 20. A Transmission Electron Micrograph of Al, 2.46 At. Percent Zn, 0.72 At. Percent Mg Alloy Aged at 135°C to Maximum Hardness. (Microscope Not Calibrated for Magnification).

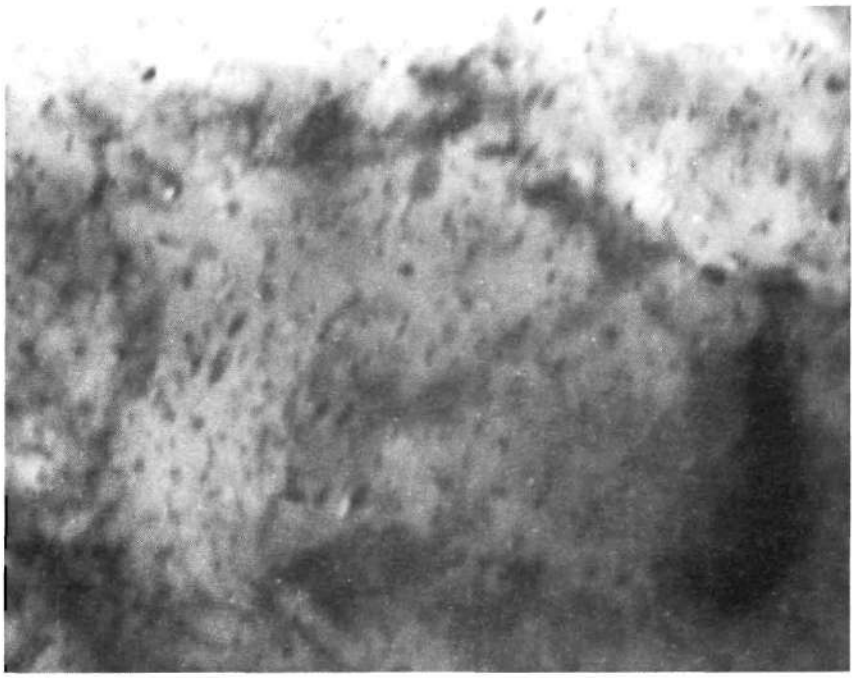

Figure 21. A Transmission Electron Micrograph of Al, 2.47 At. Percent Zn, 1.09 At. Percent Mg Alloy Aged at 135°C to Maximum Hardness. (Microscope Not Calibrated for Magnification).

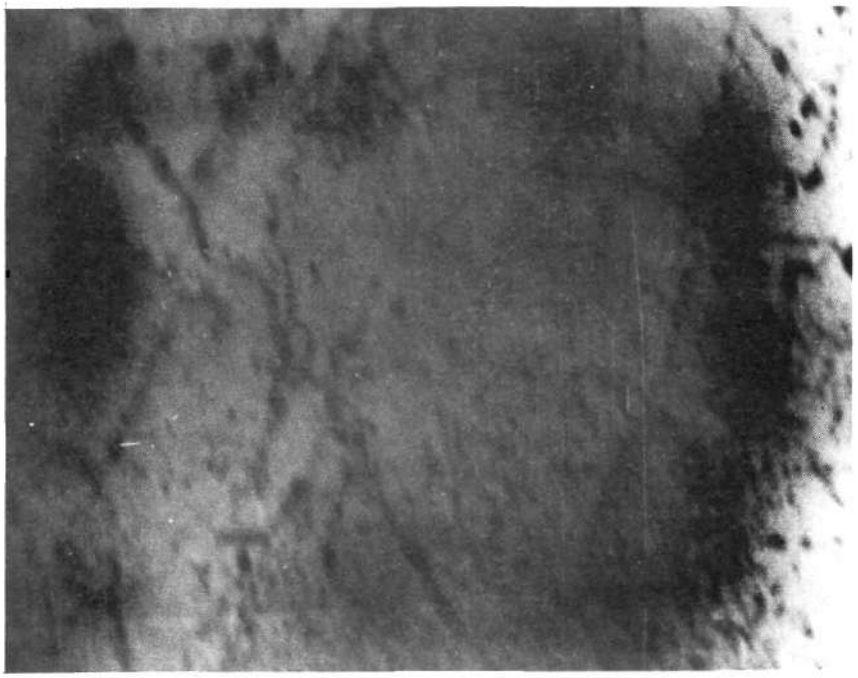

Figure 22. A Transmission Electron Micrograph Showing Dislocation Decoration by Guinier-Preston Zones in Al, 2.46 At. Percent Zn, 0.72 At. Percent Mg Alloy.

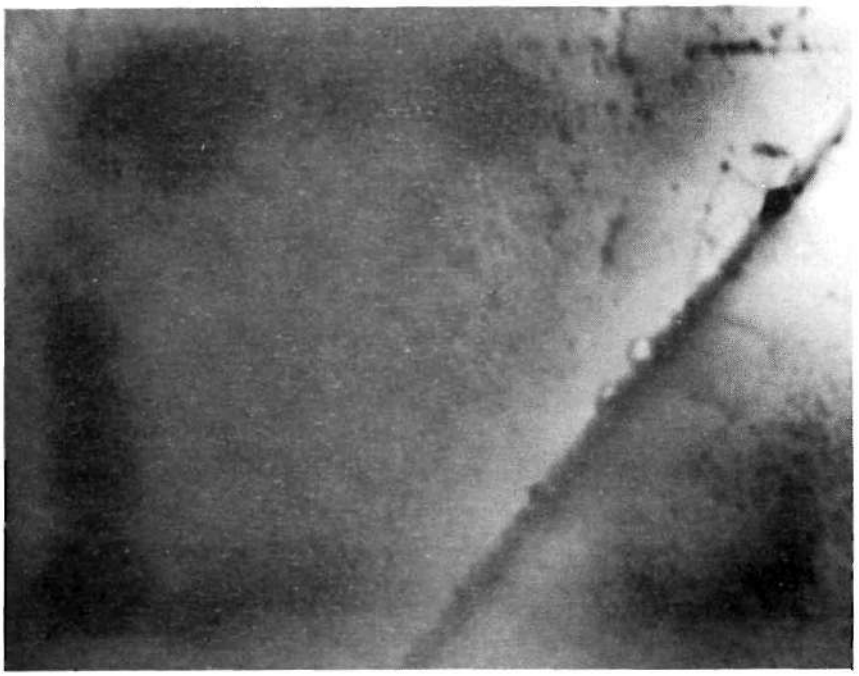

Figure 23. A Transmission Electron Micrograph Showing the Effect of Grain Boundary Precipitation in Al, 2.46 At. Percent Zn, 0.72 At. Percent Mg Alloy.

CHAPTER V

DISCUSSION OF RESULTS

In the as-quenched state the two alloys examined, Al, 2.46 percent Zn, 0.72 percent Mg and Al, 2.47 percent Zn, 1.09 percent Mg, do not appear to be wholly homogeneous. Small-angle scattering is little, suggesting that the extent of the heterogeneities formed during the quench is extremely small. The integrated intensity, Q_o, calculated from the scattering curve indicates a higher value for the 1.09 percent Mg alloy than for the 0.72 percent Mg alloy. Also, it is seen that a large as-quenched hardness difference exists which cannot be completely accounted for by the solid-solution strengthening effect of magnesium. High-angle x-ray diffraction was employed to analyze this difference. Extremely diffuse lines occurred in the 1.09 percent Mg alloy which could be attributed to $MgZn_2$. These lines were not detected when the lower magnesium alloy was examined under similar conditions. Thus, the large difference in the hardness of the two alloys in the as-quenched state is explained as being due to the following effects.

1. Solid-solution strengthening which accounts for only 5 to 6 percent of the observed 25 percent increase in hardness as the magnesium content is raised from 0.72 atomic percent to 1.09 atomic percent[40].

2. Quench clustering, whereby $MgZn_2$ clusters form during the quench in the higher Mg content alloy. Thus, the higher Q_o in the 1.09 percent alloy shows that a larger volume fraction of the quenched-in clusters occurs

in this alloy, resulting in greater hardening in this case. This phenomenon of quench-clustering also demonstrates the strong effect of small additions of magnesium on the initial clustering process.

The hardness curve for the 1.09 percent Mg alloy shows a two-stage hardening when aged at 135°C, with a linear initial stage. This fact, along with the observation of $MgZn_2$ in the as-quenched state, suggests that no nucleation barrier exists for the formation of the G-P zones in this alloy. There is a rapid growth of the zones from about 14 Å radius to 30 Å radius, resulting in the rapid hardness increase. The first stage is followed by a period of almost constant hardness. There is, however, a slight zone growth up to about a 35 Å radius, at which time the second stage is initiated. It appears that a critical zone size exists for the nucleation of η' intermediate precipitate since this precipitate accounts for the hardening in the next stage.

The appearance of the precipitate structure with resultant hardening suggests that the operative strengthening mechanism here is of a dispersion hardening type. Maximum hardening is then a result of the combination of size and spacing between the precipitates. Softening (or overageing) finally results due to coarsening of widely spaced precipitates.

The hardness curve of the 0.72 percent Mg alloy is more complex. Linear hardening is also observed in this case, but the rate of hardening is slower than in the 1.09 percent Mg alloy. A simple reason for this is that with less magnesium there are fewer magnesium-vacancy associations to aid the pre-precipitation process. At a zone size of approximately 25 Å the hardness increases more rapidly until a zone size of about 40 Å is reached, and then the hardness increase is arrested. It is observed that

after this time the zone radius remains essentially constant. The latter is an indication of the critical size required for the nucleation of η' intermediate precipitate. With further growth of the η' precipitate the second stage in the hardening curve results. No x-ray studies were made to determine the precipitate size changes once it was formed in this alloy.

Since the increase in zone radius follows closely the changes that occur in the hardness curve, it appears that a strong correlation exists between the size of the zone and the strength of the alloy. However, it must be remembered that a distribution of zone sizes always exists, as is evident from the concave nature of the Guinier plot[38]. The sudden acceleration in the hardening rate in the first stage is accompanied by a similar rapid increase in zone size. This acceleration in the ageing process is explained by using the model proposed by Perry[41].

According to Perry's theory, magnesium plays the role of a reversible vacancy trap. Since the magnesium-vacancy binding energy is extremely high compared to the zinc-vacancy binding energy in the ternary (0.17 eV as compared to 0.05 eV) most of the vacancies associated with the solute, immediately after the quench, are attached to the magnesium atoms. The vacancy concentration falls with the annihilation of the free excess vacancies at sinks, such as grain boundaries and dislocations. To maintain the supersaturated concentration of these vacancies magnesium releases the vacancies previously trapped during the quench. Thus, initially solute clusters form with the aid of isolated vacancies associated with zinc atoms. After ageing has progressed for some time the magnesium becomes activated as a vacancy source. This stage marks the accelerated ageing period prior to the incubation period for the intermediate precipitate. This model,

however, must be reconciled in some way with the fact that after the increased rate of zone growth just mentioned, further growth is suddenly arrested during the time required for the nucleation of the precipitate structure.

A further observation during the nucleation of the intermediate precipitate is that the integrated intensity is fairly constant, thus no redistribution of the solute atoms affects the nucleation and zone growth. The incubation time in this case then represents the time required to transform a fully coherent zone to a semi-coherent precipitate with a unique structure of its own. The constant zone size thus indicates that this transformation occurs only when the G-P zones have acquired a certain critical size. This observation of a critical zone size for the nucleation of the η' precipitate is consistent with the conclusion reached by Holl[26]. It does not mean, however, that all the zones have ceased to grow. The zone size obtained from the small-angle scattering data is the Guinier radius. This radius is known to be weighed in favor of the larger zones that occur in the alloy[46] since the x-ray size parameters become ratios of moments when a size distribution of particles exist. For the Kratky camera, using line-shaped beam, the exact form for the Guinier radius was derived by Baur and Gerold[46] to be:

$$R_G = \left[\frac{< R^7 >}{< R^5 >} \right]^{\frac{1}{2}}$$

where R_G is the radius determined from the Guinier approximation and $< R >$ is the mean zone radius for the distribution of sizes present. Thus, the smaller zones in the alloy keep growing while the zones which have attained

the critical size do not. The smaller zones continue to grow until the required critical size is reached.

In the hardness curve for the Mg-rich alloy an incubation period precedes the nucleation of the intermediate precipitate, η'. The parameters obtained from x-ray measurements indicate that during this stage a slight zone growth does, however, occur.

For both alloys a considerable increase in the integrated intensity is observed with time. As shown in Appendix A, the integrated intensity can be related to the volume fraction of the G-P zones and to the composition of the G-P zones. Therefore, the increase in the value of Q_o in the early stages can be a result of either an increase in the volume fraction or due to an increase in the electron density fluctuations between the matrix and the zone due to redistribution of the solute.

Gerold[42] has shown that the type of alloy being studied decomposes homogeneously and that the volume fraction of the zones remain constant. Recently, Harkness, Gould, and Hren[43] have shown that in some cases (especially in the early stages of ageing) the volume fraction of the zones may change. It is, therefore, possible that in the initial period of ageing, immediately after the quench, the increase in Q_o is due to the progress of dissociation of the alloy and the formation of the zones. At later stages it is reasonable to assume that the alloy has completely decomposed and that the volume fraction of the zones remain constant with time. The increase in Q_o is, at this stage, due only to the increased difference in the electron density of the zone and the matrix. This occurs because of the increasing concentration of the zinc in the zones.

The greater and more rapid increase in the integrated intensity in

the 1.09 percent Mg alloy is probably due to the fact that segregation is more severe than in the 0.72 percent Mg alloy, that is, the zones in the 1.09 percent Mg alloy are richer in zinc. This observation is consistent with those found by Iphorski and Bonfiglioli[44]. These workers assumed that the volume fraction of the zones does not change, an assumption necessary for the determination of the composition of the zones.

An anomalous increase in the integrated intensity was observed for the 1.09 percent Mg alloy at about the same time as the formation of the first intermediate precipitates. The formation of the small η' intermediate precipitate results in streaking (as shown by Belboech and Guinier[45]) in a manner similar to the particle size effects in high-angle diffraction. This increased scattering diminishes with the growth of η' precipitate so that Q_o decreases when the precipitate has grown sufficiently. The scattering at small angles becomes unobservable only when large and incoherent precipitates form.

CHAPTER VI

CONCLUSIONS AND RECOMMENDATIONS

Conclusions

1. Changes in the zone size follow the same pattern as the changes in hardness so that a close correlation appears to exist between the strength of these alloys with the size of the zones.

2. A critical zone size is required for the nucleation of the intermediate precipitate. The critical zone size appears to be dependent on the alloy composition; thus, for the 0.72 atomic percent magnesium alloy it is approximately 43 Å, whereas for the 1.09 atomic percent magnesium alloy it is about 33 Å. Nucleation of the intermediate precipitate is easier in the higher Mg containing alloy.

3. The role of magnesium as a reversible-vacancy trap has been established. It has also been shown that magnesium governs the concentration of zinc in the zones.

4. Higher magnesium content induces a greater extent of quench clustering, resulting in large as-quenched hardness difference in alloys having only slightly differing magnesium contents.

Recommendations for Future Studies

1. Tensile tests should be employed along with the structure characterization techniques used in the present study. This is necessary because hardness measurements yield relative changes in mechanical properties, whereas, to correlate the effect of zone size and their distribution

to the strength of the alloys in a quantitative manner yield strength data will be required.

2. At least one other ternary alloy and three other binary alloys in this system should be studied to determine the nature of the miscibility gap at elevated temperatures.

3. The changes in volume fraction of the zones with ageing should be determined by electron microscopy. In the determination of the composition of zones, workers in this area have assumed that the volume fraction of the zones remain constant.

APPENDIX A

THEORY OF SMALL ANGLE SCATTERING

Introduction

Small-angle scattering of x-rays is a phenomenon utilizing the partial diffraction of the incident beam while passing through a thin sample. Such a scattering effect occurs as a result of differences between the electron density of small regions (e.g., colloidal particles) and the matrix. From the nature of the scattering at low angles it is possible to derive information concerning the shape, size, arrangement, and volume of these small regions. The general theory and some relevant applications has been reviewed recently by Gould[48], and his treatment will be discussed briefly.

General Theory

X-ray diffraction effects that occur from a perfectly crystalline material are well separated from the direction of the incident x-ray beam and are sharply defined. On the other hand, materials having non-periodic structure or possessing a perturbed lattice give rise to extended regions of scattering in the angular ranges between successive Bragg reflections. It has also been shown that samples containing small scattering heterogeneities (of the order of 10 to 1000 times that of the incident wavelength, λ) will give rise to continuous scattering effects in the neighborhood of the primary beam. For x-rays normally used in diffraction studies (having λ = 1 to 2 Å), particles ranging from 10 to 1000 Å may be investigated.

The condition for diffraction to occur is that the reciprocal lattice node must intersect the Ewald sphere (a sphere whose radius, $\vec{S}_o/\lambda$, is directed toward the [000] node of the reciprocal space). The direction of the diffracted beam is then given by the vector $\vec{S}$ drawn from the center of the Ewald sphere to the point of contact on this sphere. A diffraction effect is always expected to occur in the direction of the primary beam, since the reciprocal lattice nodes are all identical in that there is one at (000) which corresponds to the direction of the main beam. However, in "perfect" crystals this diffraction extends to such small angles that it is not visible.

In the vicinity of the (000) region of the reciprocal space the scattered intensity I, as a function of $\vec{s}$, is given by the following relationships:

$$I(\vec{s}) = \frac{F^2}{VV_c} \Sigma(\vec{s})^2 \qquad (1)$$

where $\vec{s} = (\vec{S} - \vec{S}_o)/\lambda$ and $|\vec{s}| = (2 \sin \theta/\lambda = \epsilon/\lambda$, and F is the structure factor or the scattering ability of the unit cell. F is thus related to the electron density of the unit cell; V_c is the volume of the unit cell, and V is the irradiated volume; $\Sigma(\vec{s})$ is related to the shape of the node in reciprocal space which in turn is related to the shape of the real particle; $\Sigma(\vec{s})$ may be calculated for many regular particle shapes. For N unit cells of volume V_c, $N = V/V_c$, the intensity:

$$I_N(\vec{s}) = \frac{F^2}{VV_c} \Sigma(s)^2 \frac{V}{V_c} = \frac{F^2}{V_c^2} \Sigma(\vec{s})^2 \quad . \qquad (2)$$

Now $(F/V_c) = \rho$, the electron density, i.e., electrons per unit volume. Therefore:

$$I_N(\vec{s}) = \rho^2 \, \Sigma(\vec{s})^2 \quad . \tag{3}$$

The above is true only when the heterogeneity of electron density ρ is embedded in a matrix of zero electron density, i.e., a vacuum. In the more general case of a matrix of electron density, ρ_o, the intensity scattered by a single particle containing N unit cells can be written as:

$$I(\vec{s}) = (\rho - \rho_o)^2 \, \Sigma(\vec{s})^2 \quad . \tag{4}$$

Mathematical Model

In the following discussion it will be assumed that the heterogeneities are identical and randomly oriented. Also, the average volume occupied by each particle is large compared with the volume of the particle. Under these assumptions there is no interference of scattered x-rays between the particles, and the intensities diffracted by the various particles simply add. It is to be noted that $I(\vec{s})$ is independent of the direction of $\vec{s}$, hence $I(\vec{s}) = I(s)$, where $|\vec{s}| = s$.

To evaluate Equation (4) it is necessary to obtain the average value of $\Sigma(s)$. For spheres $\Sigma(s)$ can be shown to be:

$$\Sigma(s) = \frac{4}{3} \pi \, a^3 \, \Phi^2 \, (2\pi \, a \, s) \quad ,$$

where

$$\Phi(2\pi \, a \, s) = [3 \, (\sin 2\pi \, a \, s - 2\pi \, a \, s \cos 2\pi \, a \, s)/(2\pi \, a \, s)^3] \quad .$$

Thus, Equation (4) may be written as:

$$I(s) = \left[(\rho-\rho_o)\ \frac{4}{3}\ \pi\ a^3\right]^2 \left[\ 3\ \frac{\sin 2\pi\ a\ s\ -\ 2\pi\ a\ s\ \cos 2\pi\ a\ s}{(2\pi\ a\ s)^3}\ \right]\ .$$

Thus, the theoretical scattered intensity for such a shape may be calculated.

Guinier[39] has shown that $\Sigma(s)$ may be approximated by an exponential series if it is assumed that small-angle scattering follows a simple exponential law. The Guinier approximation is given in Equation (5) below for the spherical particles of radius r:

$$I(s) = (\rho-\rho_o)^2\ V^2\ \cdot\ \exp\left[-\ \frac{4}{5}\ \pi^2\ r^2\ s^2\ \right]\ . \qquad (5)$$

A more general form of which expresses the intensity I(s) as a function of the radius of gyration (R) of the particle is given in Equation (6) below:

$$I(s) = (\rho-\rho_o)^2\ V^2\ \cdot\ \exp\left[\ \frac{-4\pi^2\ s^2\ R^2}{3}\ \right] = n^2\ \exp\ \frac{-4\pi^2\ \epsilon^2\ R^2}{3\lambda^2}\ , \qquad (6)$$

where n is the number of elective scattered electrons and $s^2 = (\epsilon/\lambda)^2$. The radii of gyration for various shapes are known. From the above it is seen that if the logarithmic of the scattered intensity is plotted as a function of the scattering angle ϵ^2 (Equation (6)), the slope can be used to obtain R^2 directly.

The total volume of the heterogeneity can be obtained by calculating the integrated small-angle scattered intensity Q_o. It has been shown[38] that Q_o is given by:

$$Q_o = 4\pi \int_o^\infty s^2\ I(s)\ ds \qquad (7)$$

when a point-shaped beam is used. For a line-shaped beam, if t is the height of the infinitely narrow beam, this transformation becomes:

$$Q_o = 4\pi \int_o^\infty s \int_o^\infty I(s+t)\, dt\, ds \quad . \tag{8}$$

This integral represents the total scattering power in the neighborhood of the (000) node, in the first part of the reciprocal space. Also, Q_o can be related to the total volume and the volume fraction of the scattering particle in the following manner:

$$Q_o = V_a\, n_z\, V_z\, (\rho-\rho_o)^2\, (1-C_z) \quad , \tag{9}$$

where

V_a = atomic volume

n_z = number of zones per unit volume

V_z = volume of single zone

$C_z = n_z\, V_z$ = volume fraction of the zones

Measurement of Relative Absolute Intensity with a Calibrated Sample

The relative absolute intensity of a small-angle x-ray scattering is the ratio of the diffracted intensity to that of the primary beam. The techniques employed for small-angle scattering studies are mostly designed for relative measurements of intensities of the order of the scattered x-ray. Thus, the large primary beam energy cannot be simultaneously measured since, in general it exceeds the scattered radiation by several orders of

magnitude. To overcome this difficulty a pretreated Lupolen standard was used. This standard had previously been calibrated by Professor O. Kratky, as has been mentioned earlier. The calibration involved the determination of small-angle scattering of the Lupolen on an absolute scale at an angle corresponding to a Bragg value of 150 Å. This was done using the complex rotator method[35]. The absolute intensity scattered by a specimen under investigation can be determined easily by using a comparison method outlined below.

Let the primary energy weakened by the scattering sample be P_s. Then, if P_s is the energy per unit length of the primary beam weakened by the calibration sample, and the attenuation factors of the scattering and the calibration sample are A_s and A_c, respectively,

$$P_s = P_c \left[\frac{A_s}{A_c} \right] . . . . \quad . \tag{10}$$

It has been shown by Kratky[35] that,

$$P_c = \frac{1}{K} \cdot \frac{(\text{counts/min.})_c \ 150 \text{ Å}}{F} \cdot a \ . . . . \quad , \tag{11}$$

where K = constant for the calibration sample,

a = distance between sample and plane of registration, in cms.,

F = detector slit area, in cm^2.

The $(\text{counts/min.})_c$, 150 Å for the calibration sample depends on the exit and entrance slits combination used for the collimation of the primary beam and is determined separately for each combination used.

The combination of Equations (1) and (2) yields

$$P_s = \frac{1}{K} \cdot \frac{(\text{counts/min.})_c \ 150 \ \text{Å}}{F} \cdot a \cdot \frac{A_s}{A_c} \quad . \qquad (12)$$

The value of $1/(K \times A_c)$ was found to be 92.2 for the Lupolen sample used for the present investigation. By normalizing the intensity scattered at any angle by P_s, and comparing one angle with another, say at zero scattering angle, it is possible to cancel out the area F of the counting slit and thus obtain the relative absolute intensity.

APPENDIX B

SAMPLE CALCULATIONS

Zone Radius Calculations

The simplified form of Equation (6) of Appendix A is as follows:

$$R_G = \frac{1}{2\pi}\sqrt{\frac{3}{\log_{10} e}}\ \lambda\sqrt{p}$$

where R_G is the Guinier radius and p is the slope of the linear portion of the curve of log I as a function of ε^2.

For as-quenched Al, 2.46 percent Zn, 0.72 percent Mg,

$$R_G = \frac{1}{2\pi}\sqrt{\frac{3}{\log_{10} e}}\ (1.54)\sqrt{\frac{\log 82.69 - \log 30.93}{(12.01-3.37)\times 10^{-4}}} = 13.45\ \text{Å}\ .$$

Integrated Intensity Calculations

Equation (7) of Appendix A may be approximated by the following:

$$Q_o = K\left[\int_o^\infty s\ I(s)\ ds\right]$$

$$= K\int_o^\infty s\ I(s)\ ds + k\int_o^\infty s\ I(s)\ ds\ .$$

Using the asymptotic tail approximation of Porod[47] the I(s) in the

second intergral on the right is replaced by $\frac{I(s_o)\, s_o^3}{s^3}$ and the first integral is replaced by a summation. Thus, for line-shaped beam

$$Q_o = K \left[\Delta s \sum_{s=0}^{s_o} s\, E(s) + E(s_o)\, s_o^2 \right] .$$

The constant K for a sample contains certain geometrical factors and the transmission factor for the samples.

In the present calculation only the absorption factor and sample thickness have been included in K and this is .11787 for Al, 2.46 percent Zn, 0.72 percent Mg alloy and .24787 for Al, 2.47 percent Zn, 1.09 percent Mg alloy.

$\Delta s = 0.00408.$

For Al, 2.46 percent, 0.72 percent Mg in the as-quenched state, see Table 5 on the following page.

The sum of the last column in this table is as follows:

$$\Delta s \sum_{0}^{s_o} E(s) \cdot s = .280$$

$$E(s_o) \cdot s_o^2 = .206$$

$$\int_0^\infty s \cdot E(s)\, ds = .280 + .206 = .486$$

$$\therefore K \int_0^\infty s \cdot E(s)\, ds = .059 .$$

Table 5. Typical Calculation of Integrated Intensity

s	E(s)	Δs {s.E(s)}
.01021	418.83	.01745
.01439	115.83	.00675
.01836	82.69	.00619
.02244	57.49	.00526
.02651	45.50	.00492
.03050	35.06	.00436
.03466	30.93	.00437
.03874	27.37	.00433
.04282	25.56	.00447
.04689	22.24	.00425
.05097	23.25	.00483
.05504	19.63	.00441
.05912	18.51	.00446
.06319	16.27	.00419
.06727	18.06	.00495
.07134	17.20	.00501
.07542	14.56	.00448
.07949	14.41	.00467
.08357	13.23	.00451
.08764	12.51	.00447
.09172	11.68	.00437
.09579	12.94	.00506
.09987	12.00	.00489
.10395	11.45	.00486
.10803	11.80	.00520
.11211	12.00	.00548
.11617	13.16	.00623
.12025	12.5	.00613
.12433	12.5	.00633
.12841	12.4	.00649
.13249	12.4	.00670
.13655	12.5	.00696
.14063	12.3	.00706
.14471	12.1	.00715
.14879	12.0	.00729
.15287	11.9	.00742

BIBLIOGRAPHY*

1. W. Sander and K. L. Meissner, Z. Metallkunde 15, 1923, p. 181.
2. Ibid 16, 1924, p. 12.
3. W. Koster and W. Wolf, Z. Metallk 28, 1936, p. 155.
4. W. Koster and W. Dullenkopf, Z. Metallk 28, 1936, pp. 309, 363.
5. W. L. Fink and L. A. Willey, Trans. AIME 124, 1937, p. 78.
6. D. J. Stawbridge, W. Hume-Rothery, and A. T. Little, J. Inst. Met. 71, 1945, p. 291.
7. J. Herenguel and G. Chaudron, Metaux et Corrosion 16, 1941, pp. 33,49.
8. R. Graf, Compt. Rend 242, 1956, p. 1311.
9. W. Koster and K. Kam, Z. Metallk 30, 1938, p. 320.
10. I. J. Polmear, J. Inst. Met. 86, 1957-58, p. 113; Ibid 87, 1958-59, p. 24.
11. H. K. Hardy, Ibid 79, 1951, p. 321.
12. L. F. Mondolfo, N. A. Gjostein, and D. W. Levinson, J. of Metals 8, 1956, p. 378.
13. R. Graf, Compt. Rend 242, 1956, p. 1311.
14. Ibid 244, 1957, p. 337.
15. R. Graf, J. I. Metals 86, 1957-58, p. 535.
16. H. Schmalzried and V. Gerold, Z. Metallk 49, 1958, p. 291.
17. A. Guinier, Advances in Solid State Physics, Academic Press, Inc., New York, Vol. 9, 1960, p. 293.
18. R. W. Gould and E. A. Starke, Jr., Advances in X-ray Analysis, Plenum Press, Vol. 9, 1966, p. 57.

---

*Abbreviations found herein follow the form used by Nuclear Physics 1 (1956), page 539, and 7 (1958), page 299.

19. A. H. Geisler and F. Keller, Trans. AIME 171, 1947, p. 192.

20. H. Nishimura and Y. Murakami, Mem. Fac. Eng. 12, 1950, p. 47, Kyoto University.

21. Ibid 15, 1953, p. 9.

22. P. C. Varley, (Miss) M. K. B. Day, and A. Sendorek, J. Inst. Metals 86, 1957-58, p. 337.

23. R. B. Nicholson, G. Thomas, and J. Nutting, J. Inst. Metals 87, 1958-59, p. 429.

24. G. Thomas and J. Nutting, J. Inst. Metals 88, 1959-60, p. 81.

25. R. B. Nicholson, G. Thomas, and J. Nutting, Acta Met. 8, 1960, p. 172.

26. H. A. Holl, J. Inst. Metals 93, 1964-65, p. 364.

27. J. D. Embury and R. B. Nicholson, Acta Met. 13, 1965, p. 403.

28. H. Haberkorn and V. Gerold, Z. Metallkunde, 1959.

29. R. B. Nicholson, G. Thomas, and J. Nutting, Brit. J. Appl. Phys. 9, 1958, p. 75.

30. J. Taylor, J. Inst. Met. 92, 1963-64, p. 301.

31. Y. Murakami, S. Komatsu, and K. Nagata, Mem. Fac. Eng. 29, 1967, Kyoto University.

32. R. W. Gould and R. W. Hendricks, "A High and Low Temperature Sample Holder for the Kratky Camera," (accepted for publication, Review of Scientific Instruments).

33. A. Kelly and R. B. Nicholson, Precipitation Hardening - Progress in Materials Science, Pergamon Press, Vol. 10, No. 3, 1963.

34. O. Kratky, Z. Electrochemie 58, 1954, p. 49.

35. O. Kratky, I. Pilz, and P. J. Schmitz, J. Coll. & Interface Sci. 21, 1966, p. 24.

36. C. J. Sparks and B. Borie, Local Atomic Arrangements Studied by X-ray Diffraction, Gordon and Breach, Chicago, 1965, p. 3.

37. R. C. Glenn and J. C. Raley, Adv. Tech. Electron Metallography, ASTM STP 339, 1963, p. 60.

38. A. Guinier and G. Fournet, Small Angle Scattering of X-rays, New York, John Wiley & Sons, Inc., 1955.

39. A. Guinier, X-ray Diffraction, John Wiley & Sons, Inc., New York.

40. E. R. Parker and T. H. Hazlett, Relation of Properties to Microstructures, ASM, 1954.

41. A. J. Perry, Acta Met. 14, 1966, p. 1143.

42. V. Gerold, Physica Status Solids 1, 1961, p. 37.

43. S. D. Harkness, R. W. Gould, and J. J. Hren (to be published).

44. M. Iphorski and A. Bonfiglioli, J. Mat. Sci. 2, 1967, p. 371.

45. B. Belboech and A. Guinier, Acta. Met. 3, 1955, p. 370.

46. R. Baur and V. Gerold, Acta Met. 12, 1964, p. 1444.

47. G. Porod, Kolloid Z. 124, 1951, p. 83.

48. R. W. Gould, Eng. Progress University of Florida 21, 1967, p. 27.